

TABLE OF CONTENTS

LIST OF FIGURES	6
ABSTRACT	8
CHAPTER 1. INTRODUCTION	9
1.1. Synthetic Aperture Sonar (SAS) Basics	9
1.2. Problem Statement	10
1.3. Facet-Ensemble Simulations	12
1.4. Overview of Thesis	12
CHAPTER 2. BACKGROUND AND PRELIMINARY ANALYSIS	14
2.1. Mathematical Description of SAS Data	14
2.2. Form of the Multi-Path Response	16
2.3. Analysis of Multi-Path Effects on the SAS Data	18
CHAPTER 3. SEA SURFACE MODELING AND SIMULATION	21
3.1. Stochastic Sea Surface Model	21
3.2. Sea Surface Simulation Method	23
CHAPTER 4. MULTI-PATH PROPAGATION SIMULATION	26
4.1. General Facet Structure	26
4.2. Vector Framework for Facet Analysis	27
4.3. Common Facet Analysis	30
4.4. Model Specific Facet Analysis	33
4.4.1. Lambertian Model	33
4.4.2. Diffraction-Based Model	35
4.5. Constructing the Impulse Response	40
CHAPTER 5. SINGLE SURFACE SIMULATION RESULTS	43
5.1. Flat Surface Response	46
5.1.1. Lambertian Model	46
5.1.2. Diffraction-Based Model	51
5.2. Sea Surface Response	56
5.2.1. Lambertian Model	57
5.2.2. Diffraction-Based Model	59
5.3. An Intuitive Analogy	59
5.4. Model Comparison	62

TABLE OF CONTENTS—*Continued*

CHAPTER 6. MULTIPLE SURFACE SIMULATION RESULTS	64
6.1. Lambertian Model	66
6.2. Diffraction-Based Model	67
CHAPTER 7. CONCLUSIONS	70
APPENDIX A. DERIVATION OF THE FOURIER TRANSFORM OF A RIGHT- TRIANGLE	72
APPENDIX B. NOTATION GLOSSARY	75
APPENDIX C. SIMULATION CODE	80
REFERENCES	101

LIST OF FIGURES

FIGURE 1.1.	SAS system geometry	9
FIGURE 1.2.	Graphical example of multi-path propagation	11
FIGURE 3.1.	Example sea surface	25
FIGURE 4.1.	Method of facet division	26
FIGURE 4.2.	Geometry used to calculate facet returns	28
FIGURE 4.3.	Facet ray reflection angles	29
FIGURE 5.1.	Example sea surface as an image	45
FIGURE 5.2.	Gain-modulus image for a flat surface with a Lambertian scattering model	47
FIGURE 5.3.	Modulus of the impulse response for a flat surface with a Lambertian scattering model	48
FIGURE 5.4.	Phase of the impulse response for a flat surface with a Lambertian scattering model	48
FIGURE 5.5.	Gain-modulus image for a flat surface with a Lambertian scattering model and a larger facet size	50
FIGURE 5.6.	Gain-modulus image for a flat surface with a Lambertian scattering model and a shorter characteristic wavelength	51
FIGURE 5.7.	Gain-modulus image for a flat surface with a diffraction-based scattering model	52
FIGURE 5.8.	Modulus of the impulse response for a flat surface with a diffraction-based scattering model	53
FIGURE 5.9.	Phase of the impulse response for a flat surface with a diffraction-based scattering model	53
FIGURE 5.10.	Gain-modulus image for a flat surface with a diffraction-based scattering model and a larger facet size	54
FIGURE 5.11.	Gain-modulus image for a flat surface with a diffraction-based scattering model and a larger facet size synthesized by summing smaller facets	54
FIGURE 5.12.	Gain-modulus image for a flat surface with a diffraction-based scattering and a shorter characteristic wavelength	55
FIGURE 5.13.	Gain-modulus image for a sea surface with a Lambertian scattering model	57
FIGURE 5.14.	Modulus of the impulse response for a sea surface with a Lambertian scattering model	58
FIGURE 5.15.	Phase of the impulse response for a sea surface with a Lambertian scattering model	58

LIST OF FIGURES—*Continued*

FIGURE 5.16. Gain-modulus image for a sea surface with a diffraction-based scattering model	59
FIGURE 5.17. Modulus of the impulse response for a sea surface with a diffraction-based scattering model	60
FIGURE 5.18. Phase of the impulse response for a sea surface with a diffraction-based scattering model	60
FIGURE 5.19. ‘Glitter’ image for a sea surface	61
FIGURE 6.1. Set of impulse response magnitudes displayed as an image for sea surfaces with a Lambertian scattering model	64
FIGURE 6.2. Set of impulse response magnitudes for sea surfaces with a Lambertian scattering model after Stolt mapping	65
FIGURE 6.3. Target profile when including multi-path effects (Lambertian scattering model)	66
FIGURE 6.4. Set of impulse response magnitudes displayed as an image for sea surfaces with a diffraction-based scattering model	67
FIGURE 6.5. Set of impulse response magnitudes for sea surfaces with a diffraction-based scattering model after Stolt mapping	68
FIGURE 6.6. Target profile when including multi-path effects (diffraction-based scattering model)	68
FIGURE A.1. Right-triangle	72

ABSTRACT

Classical methods of analysis for Synthetic Aperture Sonar (SAS) systems do not account for any multi-path propagation effects. If multi-path effects are significant but not allowed for, they are likely to adversely affect image quality. This investigation addresses multi-path propagation from the sea surface and its effect on SAS systems. To simplify the problem, only first-order reflections from the sea surface are considered. Other effects (such as Doppler shift and reflection from bubbles) are ignored. The propagation of the acoustic signal and its scattering at the surface must be considered.

The investigation is carried out primarily through computer simulations. Sea surface functions are constructed through the realization of a stochastic model. To make the problem computationally tractable, a facet-ensemble methodology is employed when simulating the multi-path returns. Two models are examined — one treats each facet as a Lambertian reflector, and the other treats each facet as a diffracting aperture. The theory needed to perform these simulations is developed.

Both models are applied to a simulated sea surface, a flat surface and an ensemble of sea surfaces. The results are examined in terms of the physics of each model and in terms of the possible effects on SAS imaging. The characteristics of the two models are seen to vary significantly but both are shown to produce significant multi-path returns. Despite the differences in the models, the general form of the multi-path response is observed to be similar.

INVESTIGATION OF THE EFFECTS OF FIRST-ORDER, MULTI-PATH PROPAGATION FROM THE SEA SURFACE IN SYNTHETIC APERTURE SONAR SYSTEMS

Brynmor John Davis, Ph.D.
The University of Arizona, 2001

Director: Bobby R. Hunt, Ph.D.

Classical methods of analysis for Synthetic Aperture Sonar (SAS) systems do not account for any multi-path propagation effects. If multi-path effects are significant but not allowed for, they are likely to adversely affect image quality. This investigation addresses multi-path propagation from the sea surface and its effect on SAS systems. To simplify the problem, only first-order reflections from the sea surface are considered. Other effects (such as Doppler shift and reflection from bubbles) are ignored. The propagation of the acoustic signal and its scattering at the surface must be considered.

The investigation is carried out primarily through computer simulations. Sea surface functions are constructed through the realization of a stochastic model. To make the problem computationally tractable, a facet-ensemble methodology is employed when simulating the multi-path returns. Two models are examined — one treats each facet as a Lambertian reflector, and the other treats each facet as a diffracting aperture. The theory needed to perform these simulations is developed.

Both models are applied to a simulated sea surface, a flat surface and an ensemble of sea surfaces. The results are examined in terms of the physics of each model and in terms of the possible effects on SAS imaging. The characteristics of the two models are seen to vary significantly but both are shown to produce significant multi-path returns. Despite the differences in the models, the general form of the multi-path response is observed to be similar.

Chapter 1

INTRODUCTION

1.1 Synthetic Aperture Sonar (SAS) Basics

This thesis is concerned with signal propagation effects in Synthetic Aperture Sonar (SAS) systems. A brief, intuitive description of SAS systems is provided here, along with some standard terminology. See Chapter 2 for a more detailed treatment.

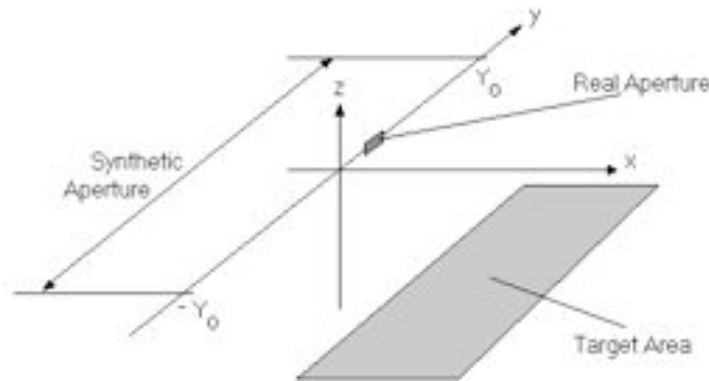


FIGURE 1.1. SAS system geometry

Sonar (radar) systems ensonify (illuminate) a target area using acoustic (electromagnetic) waves and use the echoes returned to the receiver to image the target. This thesis will investigate the sonar case, where the target area is the sea-floor or other submerged targets. Traditional systems isolate a small target subarea by using a narrow ensonifying beam. The system focuses this beam on different areas in order to build an image of the target subarea by subarea. The resolution of the resulting image is obviously determined by the size of the subareas — a narrower beam leads

to better resolution. The width of the beam is in turn defined by the size of the transmitting and receiving apertures (larger apertures lead to narrower beams.) Thus, the quality of image produced is limited by the size of the apertures.

Synthetic aperture techniques are used to circumvent this limitation. A small aperture transmits and receives signals over a range of positions. The data is collected coherently (i.e., baseband phase information is retained) and used to synthesize an image. Intuitively, data collected from several positions can be used to synthesize a return from a single larger aperture. A diagram of the basic SAS system geometry is shown in Figure 1.1.

Figure 1.1 defines a three-dimensional coordinate system (x, y, z) . The $x - y$ plane is horizontal and lies on the average sea surface level. The z dimension represents depth below the sea surface. The transmitting and receiving apertures are assumed to be coincident or nearly coincident and travel along the y -axis between $-Y_0$ and Y_0 . For this reason, the y -axis is known as the “along-track” dimension. Similarly, as the x -axis is perpendicular to the aperture path, it is known as the “cross-track” dimension.

1.2 Problem Statement

Conventional analysis of SAS signals considers the returns from targets as simply an attenuated and delayed version of the transmitted signal (see Chapter 2.) In practice this produces good results, but the images are far from perfect and the received signal is known to be more complex than stated above. It is hoped that further investigation of these more complex effects will result in an increased understanding of the limits of current SAS systems.

The particular effect to be investigated is that of multi-path propagation. Multi-path propagation occurs when reflections allow a signal to take more than one path between two points. Current methods account for only direct (line-of-sight) propaga-

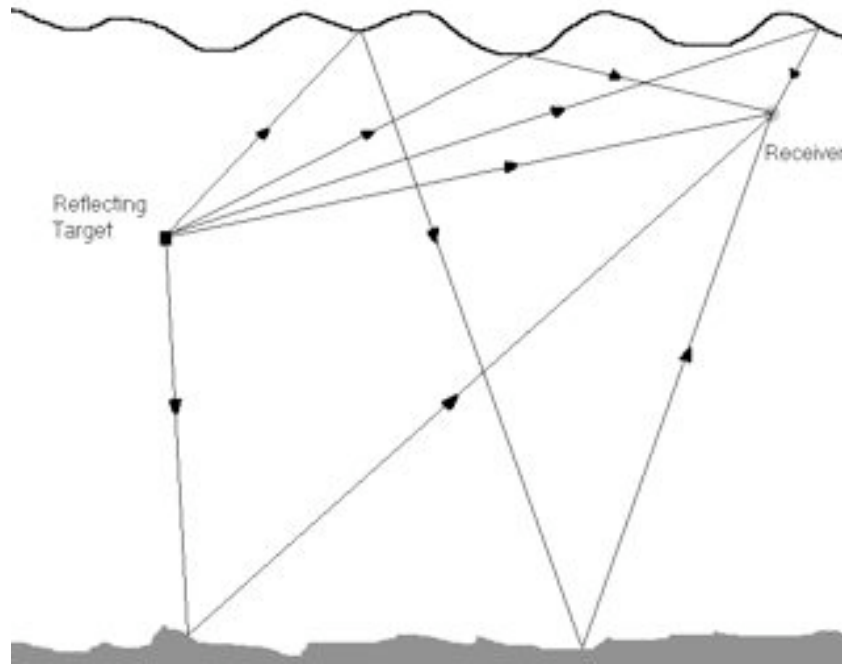


FIGURE 1.2. Graphical example of multi-path propagation

tion. In reality, more complex propagation paths must be added to this.

Figure 1.2 shows multiple paths only from the target back to the receiver. This ‘one-way’ multi-path assumption will be made throughout the investigation. Multi-path effects from the transmitter to the target are ignored because it is assumed that the transmitter has sufficient directivity to not ensonify the sea surface. In addition, it is assumed that only first-order (i.e., one reflection between target and receiver) reflections from the sea surface are significant. Essentially this means that it is assumed the target is in deep water, and any higher-order paths are attenuated to an insignificant level. For simplicity, other known effects (such as shadowing and Doppler shifts) are assumed to have negligible effect.

The ultimate goal of this investigation is to increase understanding of the effects of multi-path propagation in SAS systems. In particular the effects on the KIWI-SAS system operated by the University of Canterbury in New Zealand - see [1] and [2].

1.3 Facet-Ensemble Simulations

The aim of this investigation is to gain an insight into the acoustical signals measured by real SAS systems. However, the investigation will be pursued by means of computer simulations rather than physical experimentation. Computer simulations have the advantage of repeatability and minimal expense. In addition, computer simulations allow considerable flexibility when setting parameters such as sea state, target characteristics and SAS system configuration. Using simulations also allows theoretically useful but physically impossible situations to be investigated (e.g. reflection from a point target and removal of all effects other than multi-path propagation.) It is hoped that the results garnered from simulation methods will transfer readily into real systems.

The simulation method used is known as the facet-ensemble model. This method has a long history in the analysis of acoustical scattering from the ocean surface — see [3], [4] and [5]. The facet-ensemble model relies on dividing the rough sea surface into many small areas. These small areas can then be approximated as flat reflectors (or some other well-described scattering element.) The returns from each of the facets can then be summed to give the response from the whole sea surface. The results from this facet-ensemble method may be used to validate or refute proposed multi-path models. They may also facilitate improved intuitive understanding.

1.4 Overview of Thesis

Following this introductory chapter is a chapter containing background material and some preliminary analysis. This chapter restates some basic SAS results before incorporating a multi-path return into the same framework. The Sea Surface Modeling and Simulation chapter follows, in which an approximate sea surface is developed for computer simulation. The Multi-path Simulation chapter explains the simulation methodology and the reasoning behind it. Some results from a single sea surface are

then presented, followed by results from an ensemble of sea surfaces. Conclusions are drawn, and an appendix follows. The appendix contains the derivation of a Fourier transform used in modeling the system, a list of variables used in this thesis, and a code listing.

Chapter 2

BACKGROUND AND PRELIMINARY ANALYSIS

2.1 Mathematical Description of SAS Data

This sub-section provides a mathematical description of the signals gathered by a SAS system and is largely adapted directly from [6]. Several assumptions are made in this development, the first of which is that the target area is on the same horizontal plane as the transmit/receive apparatus. If this is not the case, it is a relatively simple transformation to shift the target plane to a level below the transmit/receive plane. Secondly, it is assumed that the transmit/receive structure is stationary during the pulse propagation (so the echo signal is received at the same location as the original signal was transmitted.) This approximation is known as the ‘hop-and-stop’ approximation as it assumes the system hops to the next transmission point, stops for transmission and reception and then hops to the next point. Thirdly, it is assumed that the receiver has a gain that increases with time. This gain is designed to undo the radius-squared spreading losses encountered ($\frac{1}{r}$ amplitude attenuation to the target and $\frac{1}{r}$ attenuation back to the receiver.) Thus the receiver has a gain of r^2 at a propagation time corresponding to a target at range r . Finally, it is assumed that the apertures have dimensions smaller than the wavelength of the transmitted signal. This means that the apertures are not directional. In [6], larger apertures are factored in after the basic development has been completed.

Let the acoustic reflectivity of the target area be given by the complex function $tt(x, y)$. The phase of $tt(x, y)$ is typically highly random which means that the Fourier transform of $tt(x, y)$ is spread over a large range of the spectrum. At this point it is appropriate to explain the double-functional notation used for $tt(x, y)$ and several functions that will be defined later. This notation allows a clear representation of

various Fourier transformations. For example, $Tt(k_x, y)$ is the Fourier transform of $tt(x, y)$ in the x direction, $tT(x, k_y)$ is the Fourier transform in the y direction and $TT(k_x, k_y)$ is the two-dimensional Fourier transform of $tt(x, y)$.

Using the preceding assumptions and notations, $dd(\alpha, y')$ will be defined as the signal collected at position y' as function of the time variable α . This data function can be written as shown below.

$$dd(\alpha, y') = \int_y \int_x tt(x, y) p\left(\alpha - \frac{2}{v_s} \sqrt{x^2 + (y - y')^2}\right) dx dy \quad (2.1)$$

With v_s being the speed of sound in water and $p(\alpha)$ being the transmitted pulse (in complex notation.) It should be noted that $p(\alpha)$ may be the raw transmitted pulse or the pulse-compressed signal. Pulse compression is performed by running the received signal through a filter matched to the transmitted pulse — this process is often done ‘on-the-fly’ in real SAS systems. Using Equation 2.1, the following relation can be derived.

$$Dd(\omega, y') = P(\omega) \int_y \int_x tt(x, y) \exp\left[-j2k\sqrt{x^2 + (y - y')^2}\right] dx dy \quad (2.2)$$

Where $k = \frac{\omega}{v_s}$. Using the principle of stationary phase allows a spatial Fourier transform to be calculated.

$$DD(\omega, k_{y'}) = P(\omega) \int_y \int_x tt(x, y) \exp\left[-j\sqrt{4k^2 - k_{y'}^2}x\right] \exp[-jk_{y'}y] dx dy \quad (2.3)$$

It should be noted that a $\sqrt{\frac{1}{4k^2 - k_{y'}^2}}$ term does arise when taking the Fourier transform of $\exp\left[-j2k\sqrt{x^2 + (y - y')^2}\right]$. This term is neglected in [6]. It is mentioned in [7] but is not included in the development. Typically $DD(\omega, k_{y'})$ is multiplied by a $\sqrt{\frac{k}{k_0}}$ factor in order to negate this unwanted term. This inversion is only approximate, but the $\sqrt{\frac{1}{4k^2 - k_{y'}^2}}$ term is generally ignored.

A coordinate transform is now used.

$$\begin{aligned} k_x(\omega, k_{y'}) &= \sqrt{4k^2 - k_{y'}^2} \\ k_y(\omega, k_{y'}) &= k_{y'} \end{aligned} \quad (2.4)$$

This coordinate change is known as the Stolt mapping and will be denoted by $\{ \cdot \}$. The final integral in Equation 2.3 can now be recognized as a 2D Fourier transform.

$$DD(\omega, k_{y'}) = P(\omega) TT(k_x, k_y) \quad (2.5)$$

In [6] it is shown that aperture effects can be incorporated as follows.

$$DD(\omega, k_{y'}) = P(\omega) A(k_{y'}) TT(k_x, k_y) \quad (2.6)$$

$A(k_{y'})$ is constructed from the Fourier transforms of the transmit and receive apertures. From Equation 2.6 it can be seen that the transmitted pulse limits the resolution in the ω direction and the apertures limit the resolution in the $k_{y'}$ direction. It should also be noted that these two limiting functions are defined on a different coordinate system to the target information. Also, the above development does not take multi-path effects into account.

2.2 Form of the Multi-Path Response

In this section a general mathematical representation of the multi-path system will be derived. Several simplifying assumptions will be made during the course of this development.

Looking at Figure 1.2, it seems logical that the multi-path response will depend on the sea surface and on the position of the target and the receiver. For simplicity it will be assumed that a single target and the receiver are at fixed locations. This means the simulations will only be valid for one target at one position but it is hoped that this will still provide insight into the system. This system geometry can also be altered to investigate different targets on subsequent runs, and the principle of superposition can be used to create multiple-target responses. The multi-path response is dependent on the sea surface which is a function of time. Thus, the multi-path system will be modeled as a linear (as the acoustical-wave system is linear), time-varying system.

In Section 2.1 the signal returned to the receiver by a single target was simply the transmitted pulse delayed by the time-of-flight. In the multi-path case this term is returned, but so are a series of attenuated and delayed echoes from the sea surface. Using the standard representation of a linear, time-varying system, the multi-path returned signal $p_M(\alpha)$ can be written as follows.

$$p_M(\alpha) = \int_{-\infty}^{\infty} p(\sigma) ee(\alpha, \sigma) d\sigma \quad (2.7)$$

Where $ee(\alpha, \sigma)$ is the response at time α to an impulse applied at time σ . Both $p(\sigma)$ and $ee(\alpha, t)$ are expressed in complex notation (i.e. amplitude and phase representation.)

For a SAS system, $p_M(\alpha)$ is generated at different y' positions (along-track locations.) The receiver will be at different y' positions at different times. Standard SAS terminology makes the distinction between ‘fast’ and ‘slow’ time. Fast time is represented by the α variable introduced in Section 2.1 — i.e. it represents the time coordinate in a single transmitted pulse. As the name suggests, slow time exists on a longer time scale. Slow time (denoted by t here) corresponds to the time measured as the system travels its along-track path. Thus, $p_M(\alpha, t)$ is the $p_M(\alpha)$ given by transmission at time t (or equivalently $p_M(\alpha, y')$ is the $p_M(\alpha)$ given at the along-track position corresponding to time t .) The function $p_M(\alpha, t)$ can be calculated by using Equation 2.7 and advancing the system t seconds.

$$p_M(\alpha, t) = \int_{-\infty}^{\infty} p(\sigma) ee(t + \alpha, t + \sigma) d\sigma \quad (2.8)$$

The duration of $p(\sigma)$ is limited to a time-scale much less than that of t (as the signal $p(\sigma)$ is transmitted and received many times over a single SAS run.) If $ee(\alpha, \sigma)$ can be approximated as time-invariant over a time-scale comparable to both $p(\sigma)$ and the range of fast-time (α) data collected on each pulse, then the following is true.

$$p_M(\alpha, t) \simeq \int_{-\infty}^{\infty} p(\sigma) ee(\alpha - \sigma, t) d\sigma \quad (2.9)$$

Where $ee(t + \alpha, t + \sigma) \simeq ee(\alpha - \sigma, t)$. The physical meaning of this approximation is to say that the sea surface can be approximated as unmoving (i.e. time-invariant) over the time it takes to transmit a single signal and receive the echoes from the target area. This is justifiable for the KIWI-SAS which transmits and receives a signal over a time period on the order of 0.1 seconds. It should be noted that this approximation removes all temporal Doppler effects.

The integral in Equation 2.9 is simply a convolution.

$$p_M(\alpha, t) = p(\alpha) *_{\alpha} ee(\alpha, t) \quad (2.10)$$

Where the $*_{\alpha}$ notation is used to explicitly indicate that the convolution is in the α dimension. Equation 2.10 can also be written as shown below.

$$p_M(\alpha, y') = p(\alpha) *_{\alpha} ee(\alpha, y') \quad (2.11)$$

Where y' is simply the along-track position at time t .

2.3 Analysis of Multi-Path Effects on the SAS Data

This subsection takes the results from Section 2.2 and incorporates them into the development in Section 2.1. The aim is to provide a mathematical description of the effect of multi-path effects on the SAS imaging system.

In Section 2.2 the multi-path system was made tractable by assuming a single target at a fixed location.

$$tt(x, y) = tt(x_0, y_0) \delta(x - x_0, y - y_0) \quad (2.12)$$

The simulations can be run for different (x_0, y_0) pairs. Using Equation 2.11 and following the steps in Section 2.1 results in the following development.

$$dd(\alpha, y') = \int_y \int_x tt(x, y) p_M\left(\alpha - \frac{2}{v_s} \sqrt{x^2 + (y - y')^2}, y'\right) dx dy \quad (2.13)$$

Taking the temporal Fourier transform. \square

$$Dd(\omega, y') = P_M(\omega, y') \int_y \int_x tt(x, y) \exp \left[-j2k\sqrt{x^2 + (y - y')^2} \right] dx dy \quad (2.14)$$

Using Equation 2.11

$$Dd(\omega, y') = P(\omega) Ee(\omega, y') \int_y \int_x tt(x, y) \exp \left[-j2k\sqrt{x^2 + (y - y')^2} \right] dx dy \quad (2.15)$$

Taking the Fourier transform with respect to y' .

$$DD(\omega, k_{y'}) = P(\omega) EE(\omega, k_{y'}) *_{k_{y'}} \int_y \int_x tt(x, y) \exp \left[-j\sqrt{4k^2 - k_{y'}^2} x \right] \exp \left[-jk_{y'} y \right] dx dy \quad (2.16)$$

Using the Stolt mapping of Equation 2.4 gives the following equation.

$$\begin{aligned} DD(\omega, k_{y'}) &= P(\omega) EE(\omega, k_{y'}) *_{k_{y'}} TT(k_x, k_y) \\ DD(\omega, k_{y'}) &= P(\omega) TT_M(k_x, k_y) \end{aligned} \quad (2.17)$$

Where $TT_M(k_x, k_y) = EE(\omega, k_{y'}) *_{k_{y'}} TT(k_x, k_y)$ represents the Fourier image of the target area after multi-path effects are included. Reconstruction algorithms start from Equation 2.5 (or Equation 2.6 when including aperture effects) and work to retrieve the target data. By looking at Equation 2.17, it can be seen that $TT_M(k_x, k_y)$ will be estimated by the reconstruction algorithms. The form of this function will be investigated as it represents the ideal reconstruction goal of traditional methods. By taking the inverse 2D Fourier transform of $TT_M(k_x, k_y)$, it is possible to find an expression for the spatial image of the target after multi-path effects are included.

$$tt_M(x, y) = ee(x, y) *_x tt(x, y) \quad (2.18)$$

It should be noted that to arrive at Equation 2.18 it was necessary to invoke the $k_{y'} = k_y$ property of the Stolt mapping and to use the relation $k = \frac{\omega}{v_s}$. The following steps are used to find $ee(x, y)$ (let \mathfrak{S} denote the Fourier transform.)

$$\begin{aligned} EE(k_x, k_y) &= \mathfrak{S} \{ EE(\omega, k_{y'}) \} && \text{(Stolt mapping)} \\ ee(x, y) &= \mathfrak{S}_{2D}^{-1} \{ EE(k_x, k_y) \} \end{aligned} \quad (2.19)$$

The Stolt mapping is not well defined over the whole frequency-plane (for example, Equation 2.4 does not give negative k_x frequencies.) For this reason, it will be necessary to carry out steps of Equation 2.19 over a limited frequency band. This band should be at least the support of the transmitted-pulse spectrum $P(\omega)$. Using this limited frequency band will cause smoothing effects but using a large band will still allow insight to be gained.

Equation 2.12 embodies the decision to evaluate the response of a single target. Substituting into Equation 2.18 gives the following expression.

$$tt_M(x, y) = tt(x_0, y_0) ee(x - x_0, y_0) \delta(y - y_0) \quad (2.20)$$

So the multi-path image of a target at (x_0, y_0) is given by Equation 2.20. It can be seen that $tt_M(x, y)$ is a scaled and shifted version of an x -axis slice of $ee(x, y)$. All that is required to evaluate Equation 2.20 is the function $ee(\alpha, y')$ (defined in Section 2.2) as this function gives $ee(x, y)$ (via the steps in Equation 2.19.) An interesting property of Equation 2.20 is that the image the SAS system produces (with multi-path effects included) is non-zero only at the along-track position equal to that of the target. It should be noted that the analysis contained in this section has not required the assumption of only investigating first order reflections.

Chapter 3

SEA SURFACE MODELING AND SIMULATION

3.1 Stochastic Sea Surface Model

In order to use a facet model it is necessary to have a description of the sea surface function $s(\hat{x}, \hat{y}, t)$, where the value of $s(\hat{x}, \hat{y}, t)$ gives the displacement from the mean surface level (the accents are to distinguish this coordinate system from (x, y, z) , which specifically represent cross-track, along-track and depth axes.) This function can be thought of as one realization of the random process $S(\hat{x}, \hat{y}, t)$ (capitalization will be used to indicate stochastic quantities.) Using this approach accounts for the uncertainty in the sea surface (i.e. the SAS system does not measure the sea surface shape, so for any given acoustic pulse the sea surface could take on any number of shapes.) While the sonar system gathers no direct readings on the sea surface, some basic a-priori properties of the surface are known (it contains a traveling wave structure dependent on wind speed.) A convenient model of these properties is given in [8]. This model is simply a correlation model of $S(\hat{x}, \hat{y}, t)$ that is based on the physics of the ocean and on experimental measurements.

It should be noted that the model defines S in windward, crosswind and time (w, c, t) coordinates. These can be easily related to the (\hat{x}, \hat{y}, t) coordinate system by defining a rotation angle ψ , which is simply a measure of the angle between wind direction and the \hat{x} -axis. Thus the model can be defined in (w, c, t) -space and converted to (\hat{x}, \hat{y}, t) -space using the following rotation transformation.

$$\begin{bmatrix} \hat{x} \\ \hat{y} \\ t \end{bmatrix} = \begin{bmatrix} \cos \psi & -\sin \psi & 0 \\ \sin \psi & \cos \psi & 0 \\ 0 & 0 & 1 \end{bmatrix} \begin{bmatrix} w \\ c \\ t \end{bmatrix} \quad (3.1)$$

The auto-correlation function that constitutes the model is given below.

$$R_S(\zeta, \eta, \tau) = A_D^2 \exp \left[\frac{-(\zeta - u_G \tau)^2}{L_w^2} \right] \exp \left[- \left(\frac{\eta}{L_c} \right)^2 \right] \cos [K_w \zeta - \tau] \quad (3.2)$$

With related variables -	ζ	Windward delay
	η	Crosswind delay
	τ	Temporal delay
	A_D	<i>R.M.S.</i> displacement amplitude
	L_w	Windward correlation length
	L_c	Crosswind correlation length
	L_t	Temporal correlation time
	K_w	Spatial frequency in windward direction
	-	Temporal frequency
	$u_G = \frac{L_x}{L_t}$	Group velocity of waves
	$u_P = \frac{1}{K_w}$	Phase velocity of waves

In addition, measurements show that the distribution of displacements at a given point is approximately Gaussian [8]. It will be assumed that the random process $S(\hat{x}, \hat{y}, t)$ is Gaussian. Stationarity is also assumed.

A small modification was made to the model outlined. It can be seen that $R_S(\zeta, \eta, \tau)$ is made up of a travelling wave (the cosine term) and two correlation decay terms. As would be expected, when $\zeta = \eta = \tau = 0$ the function is at a maximum. However, if $\eta = 0$ and $\zeta = u_G \tau$ the function has the potential (depending on the cosine) to reach the same maximum. This is meant to account for the wave-group travelling at velocity u_G but has the unreasonable property that at any separation

in time, there are two wave-crests whose correlation coefficient is 1. To remedy this problem without changing the essence of the model, a temporal window function ($win(\tau)$) was added.

$$R_S(\zeta, \eta, \tau) = A_D^2 \exp\left[\frac{-(\zeta - u_G \tau)^2}{L_w^2}\right] \exp\left[-\left(\frac{\eta}{L_c}\right)^2\right] \cos[K_w \zeta - \tau] win(\tau) \quad (3.3)$$

This model was used throughout the rest of the investigation.

3.2 Sea Surface Simulation Method

To generate a sea surface function $s(\hat{x}, \hat{y}, t)$ it is sufficient to create one realization of the random process $S(\hat{x}, \hat{y}, t)$, or equivalently of $S(w, c, t)$ (windward and crosswind coordinate system.) In order to do this it is sufficient to realize a three-dimensional Gaussian random process with an auto-correlation function as given in Equation 3.3. This can be done by passing a three-dimensional, Gaussian, white-noise process ($W(w, c, t)$) through a filter ($h(w, c, t)$.)

$$N(w, c, t) = W(w, c, t) * h(w, c, t) \quad (3.4)$$

The auto-correlation function of $N(w, c, t)$ is given below.

$$R_N(\zeta, \eta, \tau) = h(\zeta, \eta, \tau) * h(-\zeta, -\eta, -\tau) \quad (3.5)$$

So to realize $S(w, c, t)$, all that is required is to pass white, Gaussian noise through a filter that satisfies the following equation.

$$h(\zeta, \eta, \tau) * h(-\zeta, -\eta, -\tau) = R_S(\zeta, \eta, \tau) \quad (3.6)$$

$R_S(\zeta, \eta, \tau)$ is given by Equation 3.3. Equation 3.6 can be readily solved in the

Fourier domain.

$$\begin{aligned}
\mathfrak{F}[h(\zeta, \eta, \tau)] \mathfrak{F}[h(-\zeta, -\eta, -\tau)] &= \mathfrak{F}[R_S(\zeta, \eta, \tau)] \\
|\mathfrak{F}[h(\zeta, \eta, \tau)]|^2 &= \mathfrak{F}[R_S(\zeta, \eta, \tau)] \\
\mathfrak{F}[h(\zeta, \eta, \tau)] &= \sqrt{\mathfrak{F}[R_S(\zeta, \eta, \tau)]} \\
h(\zeta, \eta, \tau) &= \mathfrak{F}^{-1} \left[\sqrt{\mathfrak{F}[R_S(\zeta, \eta, \tau)]} \right] \tag{3.7}
\end{aligned}$$

The penultimate step relies on the fact that the Fourier transform of an auto-correlation function is always real and non-negative.

It is fairly straight forward to implement the methodology above using a digital computer and the FFT algorithm. One small wrinkle does occur when taking the square-root in Equation 3.7 however. It is true that the spectrum of $R_S(\zeta, \eta, \tau)$ as given in Equation 3.2 is real and greater than zero but that given in Equation 3.3 is not necessarily so. This is because of the multiplication with the window function $win(\tau)$. The effect on the spectrum of multiplying by $win(\tau)$ is to convolve the spectrum with Fourier transform of $win(\tau)$. There are possible windows with real, positive spectrums (such as the triangular window) that would not result in negative frequency components, however they may alter the form of the auto-correlation function too significantly.

In order to carry out the digital implementation it is necessary to have a finite-time auto-correlation - this means truncating $R_S(\zeta, \eta, \tau)$. So not only is there the window $win(\tau)$ present, but there are also windows in the spatial dimensions for the purposes of truncation. Intuitively, using a window that does not significantly alter the form of $R_S(\zeta, \eta, \tau)$ and doesn't truncate out significant energy should have a minimal effect on the spectrum. This is the logic that was used in the digital implementation. The Fourier transform of the digital approximation to $R_S(\zeta, \eta, \tau)$ was taken and checked for positivity. Those frequency points that were negative or complex were set to their absolute value. The energy in these points was totalled and compared to the total energy. As expected, the energy of the components in error was minimal when the

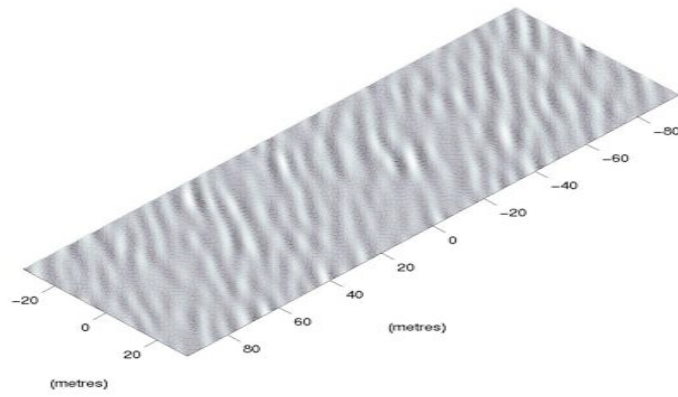


FIGURE 3.1. Example sea surface

approximation to $R_S(\zeta, \eta, \tau)$ was good. This method produced surfaces that looked credible to the eye and evolved through time in a reasonable manner. An example surface is shown in Figure 3.1

Chapter 4

MULTI-PATH PROPAGATION SIMULATION

4.1 General Facet Structure

As mentioned in Section 1.3, the facet-ensemble method works by partitioning a large complex problem into many small and simple sub-problems. By combining the solutions to these small problems, it is possible to solve the larger problem. For this application the sea surface is divided into many small facets which are then assumed to have simple reflection properties. As an acoustical-wave system is linear, the resulting reflections can then be combined by simple addition. In this manner the facet-ensemble method allows the construction of a set of multi-path, impulse responses ($ee(\alpha, t)$) from a set of sea surface functions ($s(\hat{x}, \hat{y}, t)$). It can be seen that the facet-ensemble method collapses a four-dimensional system (acoustical propagation through \hat{x} , \hat{y} , \hat{z} and α) to a two dimensional system (in α and t (fast and slow time).) Once the system is in this form it is more tractable mathematically.

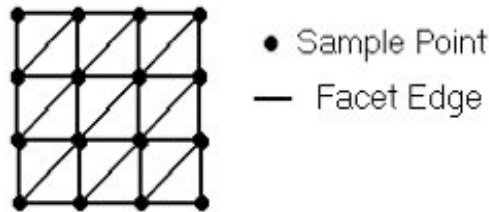


FIGURE 4.1. Method of facet division

In order to provide a comparison, two separate cases will be considered. First, each facet will be modeled as a section of a plane. This results in triangular facets, as it takes three points to define a plane. This tiling method is shown in Figure 4.1.

The simulation software was written to allow a lower-left to upper-right triangular division (as shown in Figure 4.1) or an upper-left to lower-right triangular division. The facets are assumed to completely reflect all incident sonic energy. This approximation is justified by noting the large acoustical impedance mismatch between air and water (approximate velocities are $331m.s^{-1}$ in air and $1500m.s^{-1}$ in water.) As each facet is a section of a reflecting plane, it can be equally well represented as a diffracting aperture. Fourier optics can then be used to determine how the acoustic waves are reflected.

The second method uses the same tiling method and also assumes complete reflection from the water/air boundary. However in this case each facet is assumed to have a rough surface. A phenomenon known as capillary waves are observed on real sea surfaces. Capillary waves are generated by the local wind conditions (as opposed to the large scale wind characteristics that produce the troughs and crests described by Equation 3.3.) These low amplitude capillary waves have a short spatial wavelength which can be used to justify this ‘roughness’ of the facet model. Mathematically, the roughness is accounted for by using a Lambertian reflection model for each facet. Both the Lambertian and the diffraction-based model will be discussed in detail later in this section.

4.2 Vector Framework for Facet Analysis

As an acceptable method for developing the sea surface function ($s(\hat{x}, \hat{y}, t)$) has been found and the general structure of the facet model has been established, the next step is to calculate the contribution from each facet. To simplify the mathematics, a vector system will be used to describe relevant parameters in the multi-path system. These vectors will be defined over the spatial variables $(\hat{x}, \hat{y}, \hat{z})$. The target (at depth D_t) and receiver (at depth D_r) are separated by a distance R and both lie on the \hat{y} axis. This is shown pictorially in Figure 4.2, along with the previously mentioned

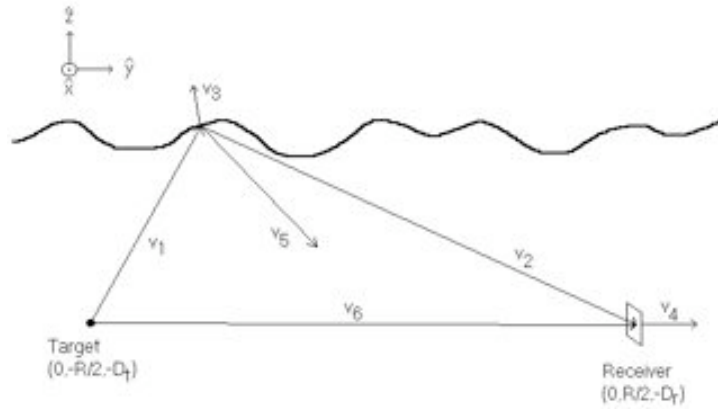


FIGURE 4.2. Geometry used to calculate facet returns

vector system. The vectors are defined as follows

- \mathbf{v}_1 Vector from target to surface
- \mathbf{v}_2 Vector from surface to receiver
- \mathbf{v}_3 Upward normal from current facet
- \mathbf{v}_4 Normal (away from target) to receiver plane
- \mathbf{v}_5 Vector pointing in the direction of a ray reflection from the facet
- \mathbf{v}_6 Vector from target to receiver

Expressions for these vectors will now be found. It is assumed that the facet of interest is at position (\hat{x}_0, \hat{y}_0) and has a displacement height of $\hat{z}_0 = s(\hat{x}_0, \hat{y}_0, t_0)$. In Section 2.2 a justification was made for taking the sea surface as unmoving over one set of returns. This is why a single temporal slice at t_0 has been taken to give the facet displacements. The coordinates (\hat{x}_0, \hat{y}_0) will be defined to be located half way between the two sample points that form the endpoints of the facet's hypotenuse (see Figure 4.1.) Similarly \hat{z}_0 is defined as the average height of the two sample points that form the endpoints of the facet's hypotenuse. From this it can be seen any facet

and its complementary facet (the one that shares a common hypotenuse) have the same location (\hat{x}_0, \hat{y}_0) and the same height \hat{z}_0 .

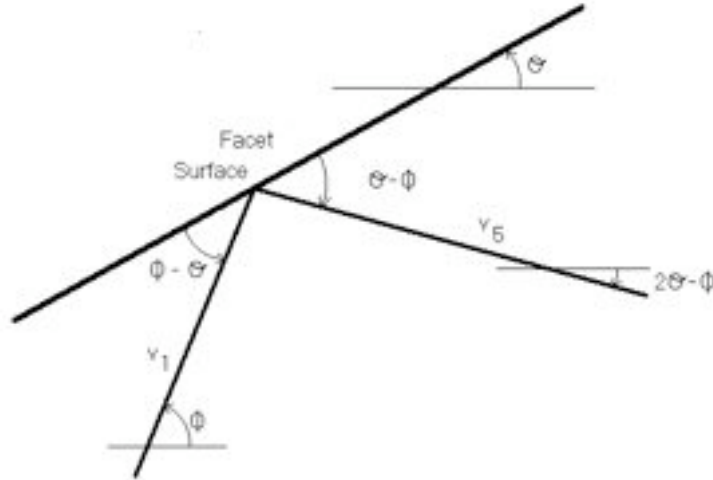


FIGURE 4.3. Facet ray reflection angles

Using this framework and referring to Figure 4.2, it is easy to find expressions for \mathbf{v}_1 and \mathbf{v}_2 .

$$\mathbf{v}_1 = \left(\hat{x}_0, \frac{R}{2} + \hat{y}_0, D_t + \hat{z}_0 \right) \quad (4.1)$$

$$\mathbf{v}_2 = \left(-\hat{x}_0, \frac{R}{2} - \hat{y}_0, -(D_r + \hat{z}_0) \right) \quad (4.2)$$

The upward normal vector \mathbf{v}_3 can be constructed using the directional slopes of the facet ($m_{\hat{x}}$ in the \hat{x} direction and $m_{\hat{y}}$ in the \hat{y} direction.) These gradients can be found from the directional tilts of the facet ($\theta_{\hat{x}}$ and $\theta_{\hat{y}}$.)

$$\mathbf{v}_3 = (-m_{\hat{x}}, -m_{\hat{y}}, 1) = (-\tan(\theta_{\hat{x}}), -\tan(\theta_{\hat{y}}), 1) \quad (4.3)$$

The normal to the receiver plane (\mathbf{v}_4) is user specified. Typically, the receiver plane is parallel to the along-track path. For example, a receiver pointed directly toward the target (azimuthally) and along the horizontal plane would give a \mathbf{v}_4 of $(0, 1, 0)$.

The vector \mathbf{v}_5 points along the ray reflection path (i.e. angle of incidence = angle of reflection and the rays stay in the plane of incidence.) Figure 4.3 shows how \mathbf{v}_5 can be calculated — the figure is only two dimensional but it is generalized to three dimensions in a straightforward manner.. Clockwise angles are positive and anti-clockwise angles are negative. The angles $\theta_{\hat{x}}$ and $\theta_{\hat{y}}$ are the same as used in the calculation of \mathbf{v}_3 . The angles $\phi_{\hat{x}}$ and $\phi_{\hat{y}}$ are the slopes of \mathbf{v}_1 in the \hat{x} and \hat{y} directions.

$$\begin{aligned}\phi_{\hat{x}} &= \tan^{-1} \left(\frac{v_{1,\hat{z}}}{v_{1,\hat{x}}} \right) = \tan^{-1} \left(\frac{D_t + \hat{z}_0}{\hat{x}_0} \right) \\ \phi_{\hat{y}} &= \tan^{-1} \left(\frac{v_{1,\hat{z}}}{v_{1,\hat{y}}} \right) = \tan^{-1} \left(\frac{D_t + \hat{z}_0}{\frac{R}{2} + \hat{y}_0} \right)\end{aligned}\quad (4.4)$$

Using basic trigonometry \mathbf{v}_5 can be calculated using the angles shown in Figure 4.3.

$$\mathbf{v}_5 = \left(\frac{\sigma}{\tan(2\theta_{\hat{x}} - \phi_{\hat{x}})}, \frac{\sigma}{\tan(2\theta_{\hat{y}} - \phi_{\hat{y}})}, \sigma \right) \quad (4.5)$$

Where σ is any real number. If σ is positive the vector will point upward, if it is negative the vector will point downward. Obviously only one of these is the true reflected path. To find which one, the vector dot-product $\mathbf{v}_3 \cdot \mathbf{v}_5$ will be taken. As the reflected path doesn't exist above the facet, σ will be chosen such that $(\mathbf{v}_3 \cdot \mathbf{v}_5)$ is negative. The absolute value of σ is arbitrarily set to one.

$$\begin{aligned}\mathbf{v}_5 &= \left(\frac{1}{\tan(2\theta_{\hat{x}} - \phi_{\hat{x}})}, \frac{1}{\tan(2\theta_{\hat{y}} - \phi_{\hat{y}})}, 1 \right) \text{ OR} \\ \mathbf{v}_5 &= - \left(\frac{1}{\tan(2\theta_{\hat{x}} - \phi_{\hat{x}})}, \frac{1}{\tan(2\theta_{\hat{y}} - \phi_{\hat{y}})}, 1 \right)\end{aligned}\quad (4.6)$$

The calculation of \mathbf{v}_6 is straightforward.

$$\mathbf{v}_6 = (0, R, D_t - D_r) \quad (4.7)$$

4.3 Common Facet Analysis

In order to create the impulse response for a given surface (i.e. $ee(\alpha, t_0)$), it is necessary to calculate a gain coefficient ($G(\hat{x}_0, \hat{y}_0)$) and a delay time ($v(\hat{x}_0, \hat{y}_0)$) for each

facet. The delay time is referenced to the arrival time for the direct (or line-of-sight) return. The propagation time from transmitter to target is fixed (as it is assumed no multi-path propagation occurs) but the propagation time from target to receiver is not. For a given facet, the difference in propagation distance is shown below.

$$\begin{aligned} d(\hat{x}_0, \hat{y}_0) &= |\mathbf{v}_1| + |\mathbf{v}_2| - |\mathbf{v}_6| \\ &= \sqrt{\mathbf{v}_1 \cdot \mathbf{v}_1} + \sqrt{\mathbf{v}_2 \cdot \mathbf{v}_2} - \sqrt{\mathbf{v}_6 \cdot \mathbf{v}_6} \end{aligned} \quad (4.8)$$

The delay time is related to $d(\hat{x}_0, \hat{y}_0)$ very simply.

$$v(\hat{x}_0, \hat{y}_0) = \frac{1}{v_s} d(\hat{x}_0, \hat{y}_0) \quad (4.9)$$

Calculating the gain coefficient is a lot more complex. There will be a $\frac{1}{|\mathbf{v}_6|}$ attenuation in pulse amplitude as it travels to the target (corresponding to a $\frac{1}{|\mathbf{v}_6|^2}$ intensity attenuation.) This will be followed by a $\frac{1}{|\mathbf{v}_1|}$ attenuation as the reflection travels to the facet. Vector calculus must then be used to determine the flux incident on the facet ($IF(\hat{x}_0, \hat{y}_0)$.)

$$IF(\hat{x}_0, \hat{y}_0) = \frac{1}{|\mathbf{v}_6|} \frac{1}{|\mathbf{v}_1|} \int_{facet} \frac{\mathbf{v}_1}{|\mathbf{v}_1|} \cdot \frac{\mathbf{v}_3}{|\mathbf{v}_3|} dS \quad (4.10)$$

The integral in Equation 4.10 is a surface integral over the facet. The normalized \mathbf{v}_1 term is a unit vector in direction of propagation and the normalized \mathbf{v}_3 vector is a unit normal. Equation 4.10 can be simplified by projecting down on to the $\hat{x} - \hat{y}$ plane. In order to do this, Equation 4.10 must be divided by the \hat{z} term of the unit normal.

$$IF(\hat{x}_0, \hat{y}_0) = \frac{1}{|\mathbf{v}_6|} \frac{1}{|\mathbf{v}_1|} \frac{|\mathbf{v}_3|}{v_{3,\hat{z}}} \int_{facet\ projection} \frac{\mathbf{v}_1}{|\mathbf{v}_1|} \cdot \frac{\mathbf{v}_3}{|\mathbf{v}_3|} d\hat{x}d\hat{y} \quad (4.11)$$

It will be assumed that the facet is small enough to allow the amplitude to be approximated as constant across its surface. The area of the facet projection is found simply by evaluating the area of a right-triangle with side lengths $\Delta\hat{x}$ and $\Delta\hat{y}$ (the

sampling periods in the \hat{x} and \hat{y} directions.)

$$\begin{aligned} IF(\hat{x}_0, \hat{y}_0) &= \frac{1}{|\mathbf{v}_6|} \frac{1}{|\mathbf{v}_1|} \frac{|\mathbf{v}_3|}{v_{3,\hat{z}}} \frac{\Delta\hat{x}\Delta\hat{y}}{2} \frac{\mathbf{v}_1}{|\mathbf{v}_1|} \cdot \frac{\mathbf{v}_3}{|\mathbf{v}_3|} \\ &= \frac{\Delta\hat{x}\Delta\hat{y}}{2} \frac{1}{|\mathbf{v}_1|^2 v_{3,\hat{z}} |\mathbf{v}_6|} (\mathbf{v}_1 \cdot \mathbf{v}_3) \end{aligned} \quad (4.12)$$

This incident flux is then scattered toward the receiver in some fashion by the facet. This scattering is model dependent (i.e. different for the diffraction model and the Lambertian model) and for the time being will simply be represented by the coefficient \square . In the next section \square will be evaluated.

The next step is to model the propagation from the facet to the receiver (which has an area of a_r .) There will be a $\frac{1}{|\mathbf{v}_2|}$ propagation loss and a flux integral at the receiver. The received flux is denoted by $RF(\hat{x}_0, \hat{y}_0)$.

$$\begin{aligned} RF(\hat{x}_0, \hat{y}_0) &= IF(\hat{x}_0, \hat{y}_0) \square \frac{1}{|\mathbf{v}_2|} \int_{receiver} \frac{\mathbf{v}_2}{|\mathbf{v}_2|} \cdot \frac{\mathbf{v}_4}{|\mathbf{v}_4|} dS \\ &= IF(\hat{x}_0, \hat{y}_0) \square \frac{1}{|\mathbf{v}_2|} a_r \frac{\mathbf{v}_2}{|\mathbf{v}_2|} \cdot \frac{\mathbf{v}_4}{|\mathbf{v}_4|} \end{aligned} \quad (4.13)$$

It has been assumed that the receiver area is small enough to allow the incident flux to be modeled as a constant. The actual value of the receiver area (a_r) is a constant by which every return will be multiplied. The analysis of Section 2.1 has neglected any such constants as they do not effect the end image (which will be normalized to some range.) For this reason, the a_r term will be dropped.

Equation 4.12 can be substituted into Equation 4.13.

$$RF(\hat{x}_0, \hat{y}_0) = \square \frac{\Delta\hat{x}\Delta\hat{y}}{2} \frac{1}{|\mathbf{v}_1|^2 |\mathbf{v}_2|^2 v_{3,\hat{z}} |\mathbf{v}_4| |\mathbf{v}_6|} (\mathbf{v}_1 \cdot \mathbf{v}_3) (\mathbf{v}_2 \cdot \mathbf{v}_4) \quad (4.14)$$

To get the gain term $G(\hat{x}_0, \hat{y}_0)$ it is necessary to multiply $RF(\hat{x}_0, \hat{y}_0)$ by the time-varying gain of the receiver (as mentioned in Section 2.1.) This gain term is twice the range that the receiver perceives the signal to have come from. A facet with delay $d(\hat{x}_0, \hat{y}_0)$ will be perceived to correspond to a target at a range of $\frac{d(\hat{x}_0, \hat{y}_0) + 2|\mathbf{v}_6|}{2}$ as the

signal travels $|\mathbf{v}_6|$ to the target and $d(\hat{x}_0, \hat{y}_0) + |\mathbf{v}_6|$ back to the receiver.

$$G(\hat{x}_0, \hat{y}_0) = \left(|\mathbf{v}_6| + \frac{d(\hat{x}_0, \hat{y}_0)}{2} \right)^2 \square \frac{\Delta \hat{x} \Delta \hat{y}}{2} \times \frac{1}{|\mathbf{v}_1|^2 |\mathbf{v}_2|^2 v_{3,\hat{z}} |\mathbf{v}_4| |\mathbf{v}_6|} (\mathbf{v}_1 \cdot \mathbf{v}_3) (\mathbf{v}_2 \cdot \mathbf{v}_4) \quad (4.15)$$

It should be noted that this gain term does not account for effects such as occlusions or reflections from bubbles.

4.4 Model Specific Facet Analysis

In order to fully evaluate $G(\hat{x}_0, \hat{y}_0)$ it is necessary to find an expression for \square (the attenuation due to scattering.) As mentioned earlier, this factor will differ for the two models used (the Lambertian model and the diffraction-based model.)

4.4.1 Lambertian Model

As mentioned earlier, the Lambertian model is used when the facets are considered to be rough. This model is simple and commonly used for modelling scattering from a rough surface [9]. The Lambertian model is an intensity model. As amplitude calculations are being performed here, some modifications will need to be made.

If a field of intensity 1 is incident on a Lambertian surface (with 100% reflectivity), the following equation describes the distribution of the reflected energy.

$$I = \frac{\cos \varphi}{\pi} \quad (4.16)$$

Where φ is the angle between the out-going ray path and the surface normal. The factor of π ensures that energy is conserved. Spreading losses have been removed from this equation as they are already accounted for in Equation 4.15.

Taking the square-root of Equation 4.16 results in an expression for the modulus of the scattered amplitude

$$|\square| = \sqrt{\frac{1}{\pi}} \sqrt{\cos \varphi} = \sqrt{\frac{1}{\pi}} \sqrt{\frac{(\mathbf{v}_2 \cdot -\mathbf{v}_3)}{|\mathbf{v}_2| |\mathbf{v}_3|}} \quad (4.17)$$

As Equation 4.17 shows, $\cos \varphi$ is readily expressed in terms of the vector system developed (as $(\mathbf{v}_2 \cdot -\mathbf{v}_3) = |\mathbf{v}_2| |\mathbf{v}_3| \cos \varphi$.)

It was decided to assign a phase to \square that corresponded to the phase delay induced by propagation over a distance of $\sqrt{|\mathbf{v}_1|^2 + |\mathbf{v}_2|^2}$ (i.e. the length of the propagation path from target to receiver.) Obviously this phase delay is dependent upon the wavelength of the signal. A representative wavelength λ was assumed. A reasonable value for this parameter could be determined by the carrier frequency of the transmitted signal.

$$\lambda = \frac{2\pi v_s}{\omega_c} \quad (4.18)$$

Where ω_c is the carrier frequency. Defining a representative wavelength has the potential to be an over-simplification, especially as the majority of signals used in SAS imagery are wide-band chirp signals. This simplification does produce a well defined phase for \square however.

$$\angle \square = \exp \left[j \frac{2\pi}{\lambda} (|\mathbf{v}_1| + |\mathbf{v}_2|) \right] \quad (4.19)$$

Combining Equation 4.17 and Equation 4.19 results in the following equation.

$$\square = \sqrt{\frac{1}{\pi}} \sqrt{\frac{1}{|\mathbf{v}_2| |\mathbf{v}_3|}} \sqrt{(\mathbf{v}_2 \cdot -\mathbf{v}_3)} \exp \left[j \frac{2\pi}{\lambda} (|\mathbf{v}_1| + |\mathbf{v}_2|) \right] \quad (4.20)$$

Combining Equation 4.15 and Equation 4.20 gives an expression for the Lambertian facet gain $G_L(\hat{x}_0, \hat{y}_0)$.

$$G_L(\hat{x}_0, \hat{y}_0) = \left(|\mathbf{v}_6| + \frac{d(\hat{x}_0, \hat{y}_0)}{2} \right)^2 \frac{\Delta \hat{x} \Delta \hat{y}}{2\sqrt{\pi}} \exp \left[j \frac{2\pi}{\lambda} (|\mathbf{v}_1| + |\mathbf{v}_2|) \right] \times \frac{1}{|\mathbf{v}_1|^2 |\mathbf{v}_2|^{\frac{5}{2}} \sqrt{|\mathbf{v}_3|} v_{3,\hat{z}} |\mathbf{v}_4| |\mathbf{v}_6|} (\mathbf{v}_1 \cdot \mathbf{v}_3) \sqrt{(\mathbf{v}_2 \cdot -\mathbf{v}_3)} (\mathbf{v}_2 \cdot \mathbf{v}_4) \quad (4.21)$$

By following the development of Equation 4.21, it can be seen that the inner product terms come from the calculation of $|G_L(\hat{x}_0, \hat{y}_0)|$ and consequently should be positive. This can be justified for physical reasons too.

$(\mathbf{v}_1 \cdot \mathbf{v}_3) < 0 \implies$ The ray is striking the facet from above the surface.

$(\mathbf{v}_2 \cdot -\mathbf{v}_3) < 0 \implies$ The path to the receiver passes through the surface.

$(\mathbf{v}_2 \cdot \mathbf{v}_4) < 0 \implies$ The facet is behind the receiver.

In of these cases the facet is either occluded ($(\mathbf{v}_1 \cdot \mathbf{v}_3) < 0$) or would not scatter any energy to the receiver. This leads to the following condition.

$$\begin{aligned} & \text{If } (\mathbf{v}_1 \cdot \mathbf{v}_3) < 0 \text{ or } (\mathbf{v}_2 \cdot -\mathbf{v}_3) < 0 \text{ or } (\mathbf{v}_2 \cdot \mathbf{v}_4) < 0 \\ & \text{then } G_L(\hat{x}_0, \hat{y}_0) = 0 \end{aligned} \quad (4.22)$$

4.4.2 Diffraction-Based Model

This model uses Fourier optics to find the scattering attenuation \square . As each facet is being treated separately, each facet can be considered as an aperture being ensonified by a source. This system must be set up so that the amplitude function across the aperture is equal to that produced by ensonification from the return from the target. The system will be analyzed at the single wavelength λ (as in Section 4.4.1.) The same accuracy concerns (regarding the single wavelength approximation) as in Section 4.4.1 apply here.

The modulus of the amplitude across the facet aperture has been accounted for in Equation 4.15. The phase across the aperture and the resultant scattering pattern must be determined. The first step in doing this is to rotate the facet into a convenient coordinate system. A coordinate rotation can be performed by pre-multiplication by a matrix $\overline{\overline{\Psi}}$, whose rows are orthonormal vectors. The rotation defined here will take the facet from $(\hat{x}, \hat{y}, \hat{z})$ coordinates to $(\tilde{x}, \tilde{y}, \tilde{z})$ coordinates.

$$\overline{\overline{\Psi}} \begin{bmatrix} \hat{x} \\ \hat{y} \\ \hat{z} \end{bmatrix} = \begin{bmatrix} \tilde{x} \\ \tilde{y} \\ \tilde{z} \end{bmatrix} \quad (4.23)$$

The first requirement of the rotation will be that it rotates the facet's downward-normal to lie along one axis. This means one row of $\overline{\overline{\Psi}}$ must be the normalized

downward facet normal. As the facet edges running along the \hat{x} - and \hat{y} -axis are orthogonal to the facet downward-normal, it will be possible to define the rotation such that one of these edges also runs along an axis in $(\tilde{x}, \tilde{y}, \tilde{z})$ space. The edge running along the \hat{y} -axis will be chosen as low grazing angles are predominantly in the \hat{y} -direction and the scattering functions are more sensitive to small changes at low grazing angles. So one row of $\overline{\overline{\Psi}}$ is a normalized version of a vector running along the \hat{y} edge. The Gram-Schmidt orthonormalization procedure can then be used to find a normalized vector orthogonal to both the downward normal and the \hat{y} edge. Before this is done, two useful terms will be defined. The quantity $\Delta\hat{z}_{\hat{x}}$ is the change in sea surface displacement along the facet edge parallel to the \hat{x} -axis. Similarly, $\Delta\hat{z}_{\hat{y}}$ is the change in sea surface displacement along the facet edge parallel to the \hat{y} -axis.

The facet downward-normal vector (\mathbf{fn}) is simply $-\mathbf{v}_3$.

$$\begin{aligned}\mathbf{fn} &= -\mathbf{v}_3 \\ &= (m_{\hat{x}}, m_{\hat{y}}, -1) \\ &= \left(\frac{\Delta\hat{z}_{\hat{x}}}{\Delta\hat{x}}, \frac{\Delta\hat{z}_{\hat{y}}}{\Delta\hat{y}}, -1 \right)\end{aligned}\quad (4.24)$$

Vectors representing the facet edges ($\mathbf{fe}_{\hat{x}}$ and $\mathbf{fe}_{\hat{y}}$) are also easily defined

$$\mathbf{fe}_{\hat{x}} = (\Delta\hat{x}, 0, \Delta\hat{z}_{\hat{x}}) \quad (4.25)$$

$$\mathbf{fe}_{\hat{y}} = (0, \Delta\hat{y}, \Delta\hat{z}_{\hat{y}}) \quad (4.26)$$

By examining Equations 4.24, 4.25 and 4.26, it can be seen that the downward normal is indeed orthogonal to both edge vectors.

As mentioned earlier, two rows of the rotation matrix $\overline{\overline{\Psi}}$ will be given by $\frac{\mathbf{fn}}{|\mathbf{fn}|}$ and $\frac{\mathbf{fe}_{\hat{y}}}{|\mathbf{fe}_{\hat{y}}|}$ and the third row ($\overline{\overline{\Psi}}_3$) must be orthogonal to both of these. Using Gram-Schmidt, a vector (\mathbf{fe}_{orth}) was constructed to be orthogonal to $\frac{\mathbf{fn}}{|\mathbf{fn}|}$ and $\frac{\mathbf{fe}_{\hat{y}}}{|\mathbf{fe}_{\hat{y}}|}$. \mathbf{fe}_{orth} represents an edge of a facet that is a right-triangle, has another edge given by $\mathbf{fe}_{\hat{y}}$ and a downward normal \mathbf{fn} .

$$\mathbf{fe}_{orth} = \left(\Delta\hat{x}, \frac{-\Delta\hat{y}\Delta\hat{z}_{\hat{x}}\Delta\hat{z}_{\hat{y}}}{\Delta\hat{y}^2 + \Delta\hat{z}_{\hat{y}}^2}, \Delta\hat{z}_{\hat{x}} - \frac{\Delta\hat{z}_{\hat{x}}\Delta\hat{z}_{\hat{y}}^2}{\Delta\hat{y}^2 + \Delta\hat{z}_{\hat{y}}^2} \right) \quad (4.27)$$

This now allows the rotation matrix to be defined.

$$\overline{\overline{\Psi}} = \begin{bmatrix} \frac{\mathbf{fe}_{orth}}{|\mathbf{fe}_{orth}|} \\ \frac{\mathbf{fe}_{\hat{y}}}{|\mathbf{fe}_{\hat{y}}|} \\ \frac{\mathbf{fn}}{|\mathbf{fn}|} \end{bmatrix} \quad (4.28)$$

By comparing Equation 4.25 to Equation 4.27, it can be seen that if $\Delta\hat{z}_{\hat{x}}$ and $\Delta\hat{z}_{\hat{y}}$ are small in comparison to $\Delta\hat{x}$ and $\Delta\hat{y}$, then $\mathbf{fe}_{\hat{x}} \simeq \mathbf{fe}_{orth}$. This condition will be met in a real system as the slope of the sea surface is relatively small, which means $\Delta\hat{z}_{\hat{x}}$ and $\Delta\hat{z}_{\hat{y}}$ are small in comparison to $\Delta\hat{x}$ and $\Delta\hat{y}$. This leads to the following approximation.

$$\overline{\overline{\Psi}} \begin{bmatrix} \mathbf{fe}_{\hat{x}}^T & \mathbf{fe}_{\hat{y}}^T & \mathbf{fn}^T \end{bmatrix} \simeq \begin{bmatrix} |\mathbf{fe}_{\hat{x}}| & 0 & 0 \\ 0 & |\mathbf{fe}_{\hat{y}}| & 0 \\ 0 & 0 & |\mathbf{fn}| \end{bmatrix} \quad (4.29)$$

This approximation means the rotation matrix $\overline{\overline{\Psi}}$ takes the facet to a right-triangle in the $\tilde{x} - \tilde{y}$ plane. The rotation will also be applied to the vectors \mathbf{v}_1 , \mathbf{v}_2 and \mathbf{v}_5 .

$$\overline{\overline{\Psi}} \begin{bmatrix} \mathbf{v}_1^T & \mathbf{v}_2^T & \mathbf{v}_5^T \end{bmatrix} = \begin{bmatrix} \tilde{\mathbf{v}}_1^T & \tilde{\mathbf{v}}_2^T & \tilde{\mathbf{v}}_5^T \end{bmatrix} \quad (4.30)$$

The incident field in the vicinity of the facet can be approximated as a plane wave. So the phase can be written as shown below.

$$\angle IF(\tilde{x}, \tilde{y}, \tilde{z}) = \exp \left[j \frac{2\pi}{\lambda} (\mu_{\tilde{x}}(\tilde{x} - \tilde{x}_t) + \mu_{\tilde{y}}(\tilde{y} - \tilde{y}_t) + \mu_{\tilde{z}}(\tilde{z} - \tilde{z}_t)) \right] \quad (4.31)$$

Where $(\tilde{x}_t, \tilde{y}_t, \tilde{z}_t)$ is the target position in $(\tilde{x}, \tilde{y}, \tilde{z})$ coordinates and the following definition holds.

$$\frac{\tilde{\mathbf{v}}_1}{|\tilde{\mathbf{v}}_1|} = (\mu_{\tilde{x}}, \mu_{\tilde{y}}, \mu_{\tilde{z}}) \quad (4.32)$$

The facet is located at $(\tilde{x}_0, \tilde{y}_0, \tilde{z}_0)$ (found by applying $\overline{\overline{\Psi}}$ to $(\hat{x}_0, \hat{y}_0, \hat{z}_0)$) and lies in the $\tilde{x} - \tilde{y}$ plane. This means the phase across the aperture can be written as shown

below.

$$\begin{aligned}
\angle IF(\tilde{x}, \tilde{y}) &= \exp \left[j \frac{2\pi}{\lambda} (\mu_{\tilde{x}} (\tilde{x}_0 - \tilde{x}_t) + \mu_{\tilde{y}} (\tilde{y}_0 - \tilde{y}_t) + \mu_{\tilde{z}} (\tilde{z}_0 - \tilde{z}_t)) \right] \\
&\times \exp \left[j \frac{2\pi}{\lambda} (\mu_{\tilde{x}} (\tilde{x} - \tilde{x}_0) + \mu_{\tilde{y}} (\tilde{y} - \tilde{y}_0)) \right] \\
&= \exp \left[j \frac{2\pi}{\lambda} |\mathbf{v}_1| \right] \exp \left[j \frac{2\pi}{\lambda} (\mu_{\tilde{x}} (\tilde{x} - \tilde{x}_0) + \mu_{\tilde{y}} (\tilde{y} - \tilde{y}_0)) \right] \quad (4.33)
\end{aligned}$$

It can be seen that Equation 4.33 has been written in a form that places the facet at the origin ($(\tilde{x} - \tilde{x}_0)$ and $(\tilde{y} - \tilde{y}_0)$ coordinates.) Appendix A contains the derivation of the Fourier transform of a facet with zero phase across it and dimensions $\Delta\hat{x}$ and $\Delta\hat{y}$ - this Fourier transform is denoted by $F(\omega_{\tilde{x}}, \omega_{\tilde{y}})$. The Fourier transform of a facet (with zero phase and at the origin) with dimensions $|\mathbf{fe}_{\hat{x}}|$ and $|\mathbf{fe}_{\hat{y}}|$ (given by Equation 4.29) can be found using basic properties of the Fourier transform.

$$FA(\omega_{\tilde{x}}, \omega_{\tilde{y}}) = \frac{|\mathbf{fe}_{\hat{x}}|}{\Delta\hat{x}} \frac{|\mathbf{fe}_{\hat{y}}|}{\Delta\hat{y}} F\left(\frac{|\mathbf{fe}_{\hat{x}}|}{\Delta\hat{x}}(\pm\omega_{\tilde{x}}), \frac{|\mathbf{fe}_{\hat{y}}|}{\Delta\hat{y}}(\pm\omega_{\tilde{y}})\right) \quad (4.34)$$

The \pm terms account for the different faceting methods. There are four possible facet orientations which corresponds to the four possible functions obtainable from Equation 4.34. Including the phase of Equation 4.33 gives the Fourier transform of the facet aperture function.

$$FA_P(\omega_{\tilde{x}}, \omega_{\tilde{y}}) = \exp \left[j \frac{2\pi}{\lambda} |\mathbf{v}_1| \right] FA\left(\omega_{\tilde{x}} - \frac{2\pi\mu_{\tilde{x}}}{\lambda}, \omega_{\tilde{y}} - \frac{2\pi\mu_{\tilde{y}}}{\lambda}\right) \quad (4.35)$$

Fourier optics can now be used to calculate the field at the receiver. First define the following unit vector.

$$\frac{\tilde{\mathbf{v}}_2}{|\tilde{\mathbf{v}}_2|} = (\rho_{\tilde{x}}, \rho_{\tilde{y}}, \rho_{\tilde{z}}) \quad (4.36)$$

If the receiver is located at $(\tilde{x}_r, \tilde{y}_r, \tilde{z}_r)$ in $(\tilde{x}, \tilde{y}, \tilde{z})$ coordinates then the following result holds.

$$\rho_{\tilde{x}} = \frac{\tilde{x}_r - \tilde{x}_0}{|\tilde{\mathbf{v}}_2|} \quad (4.37)$$

$$\rho_{\tilde{y}} = \frac{\tilde{y}_r - \tilde{y}_0}{|\tilde{\mathbf{v}}_2|} \quad (4.38)$$

Note that the distances above are referenced to the facet position. Fourier Optics and in particular Fraunhofer diffraction (see [10]) can now be applied to give the field at the receiver.

$$\begin{aligned}\square &= \frac{\exp\left[j\frac{2\pi}{\lambda}|\mathbf{v}_2|\right]}{j\lambda} F A_P\left(\frac{2\pi\rho_{\tilde{x}}}{\lambda}, \frac{2\pi\rho_{\tilde{y}}}{\lambda}\right) \\ &= \frac{\exp\left[j\frac{2\pi}{\lambda}(|\mathbf{v}_1| + |\mathbf{v}_2|)\right]}{j\lambda} F A\left(\frac{2\pi(\rho_{\tilde{x}} - \mu_{\tilde{x}})}{\lambda}, \frac{2\pi(\rho_{\tilde{y}} - \mu_{\tilde{y}})}{\lambda}\right)\end{aligned}\quad (4.39)$$

The term accounting for propagation loss has been left out of Equation 4.39 as it is accounted for in Equation 4.15. Substituting \square (as it is defined in Equation 4.39) into Equation 4.15 gives the following expression for the gain when using the diffraction model ($G_D(\hat{x}_0, \hat{y}_0)$.)

$$\begin{aligned}G_D(\hat{x}_0, \hat{y}_0) &= \left(|\mathbf{v}_6| + \frac{d(\hat{x}_0, \hat{y}_0)}{2}\right)^2 \frac{\Delta\hat{x}\Delta\hat{y} \exp\left[j\frac{2\pi}{\lambda}(|\mathbf{v}_1| + |\mathbf{v}_2|)\right]}{2 j\lambda} \times \\ &\quad F A\left(\frac{2\pi(\rho_{\tilde{x}} - \mu_{\tilde{x}})}{\lambda}, \frac{2\pi(\rho_{\tilde{y}} - \mu_{\tilde{y}})}{\lambda}\right) \times \\ &\quad \frac{1}{|\mathbf{v}_1|^2 |\mathbf{v}_2|^2 v_{3,\tilde{z}} |\mathbf{v}_4| |\mathbf{v}_6|} (\mathbf{v}_1 \cdot \mathbf{v}_3) (\mathbf{v}_2 \cdot \mathbf{v}_4)\end{aligned}\quad (4.40)$$

It should be noted that $F A(\omega_{\tilde{x}}, \omega_{\tilde{y}})$ is at its maximum at $(0, 0)$ (this is true of the Fourier transform of any positive function.) This means that \square will be at a maximum when $\rho_{\tilde{x}} = \mu_{\tilde{x}}$ and $\rho_{\tilde{y}} = \mu_{\tilde{y}}$. This can be justified intuitively. Referring back to Equation 4.30, Equation 4.32 and the laws of reflection the following can be seen.

$$\frac{\tilde{\mathbf{v}}_5}{|\tilde{\mathbf{v}}_5|} = (\mu_{\tilde{x}}, \mu_{\tilde{y}}, -\mu_{\tilde{z}})\quad (4.41)$$

Equation 4.41 defines the path of a reflected ray (\mathbf{v}_5) from the path of the incident ray (\mathbf{v}_1 .) So when the receiver (located by \mathbf{v}_2) lies along the path of the reflected ray, $\rho_{\tilde{x}} = \mu_{\tilde{x}}$, $\rho_{\tilde{y}} = \mu_{\tilde{y}}$ (Equation 4.36 defines $\rho_{\tilde{x}}$ and $\rho_{\tilde{y}}$) and the scattered amplitude will be at a maximum.

The checks of Equation 4.22 will be applied for the same reasons as given in Section 4.4.1.

The calculation of $G_D(\hat{x}_0, \hat{y}_0)$ is a long process so the steps will be briefly restated. First the rotation matrix $\overline{\overline{\Psi}}$ is calculated from the sample points. This matrix transformation is applied to the vectors \mathbf{v}_1 (or \mathbf{v}_5) and \mathbf{v}_2 (which gives the variables $\rho_{\tilde{x}}$, $\rho_{\tilde{y}}$, $\mu_{\tilde{x}}$ and $\mu_{\tilde{y}}$.) The sample points are used to calculate the facet edge lengths $|\mathbf{fe}_{\tilde{x}}|$ and $|\mathbf{fe}_{\tilde{y}}|$ which are then used to calculate $FA(\omega_{\tilde{x}}, \omega_{\tilde{y}})$. These variables and the framework of Sections 4.2 and 4.3 allow $G_D(\hat{x}_0, \hat{y}_0)$ to be calculated (using Equation 4.40.)

4.5 Constructing the Impulse Response

Now that each facet has been assigned a delay time $v(\hat{x}_0, \hat{y}_0)$ (Equation 4.9) and a gain term $G(\hat{x}_0, \hat{y}_0)$ (Equation 4.21 or Equation 4.40), the impulse response $ee(\alpha, t_0)$ can be constructed. As this process is being carried out digitally, a sampling period for $ee(\alpha, t_0)$ will have to be found. Each sample in the impulse response has the effect of adding an attenuated and delayed version of the transmitted pulse. For this sampled function to adequately represent the continuous case, the transmitted signal should vary little over the sampling period (denoted by $\Delta\alpha$.) A representative figure for how fast the signal changes is the central (or carrier) frequency ω_c — the larger ω_c is, the faster the signal varies. So the sampling period can be set as given below.

$$\Delta\alpha = \frac{1}{C_S\omega_c} \quad (4.42)$$

Where C_S is a sampling constant.

An alternative way of approaching this problem is to consider a Nyquist approach. It is possible that the impulse response $ee(\alpha, t_0)$ has a highly variable phase and thus a very large bandwidth. However, $ee(\alpha, t_0)$ is convolved with $p(\alpha)$ to get the received signal (Equation 2.9.) This means the resultant bandwidth will be limited to that of $p(\alpha)$. Thus it is only necessary to adequately represent the frequency components of $ee(\alpha, t_0)$ falling within this bandwidth. The Nyquist sampling theorem states that

the sampling rate ($\frac{1}{\Delta\alpha}$) must be at least twice the highest frequency present. This highest frequency can be written as ($\frac{\omega_c}{2\pi} + \frac{BW}{2}$) (using Hertz rather than angular frequency and letting BW denote the baseband bandwidth of $p(\alpha)$.) Applying the Nyquist sampling theorem gives the following result.

$$\frac{1}{\Delta\alpha} \geq 2 \left(\frac{\omega_c}{2\pi} + \frac{BW}{2} \right) \quad (4.43)$$

So Equation 4.43 gives a minimum requirement on C_S . However, it should be noted that the discrete version of $ee(\alpha, t_0)$ (denoted by $ee_D(n\Delta\alpha, t_0)$) is not constructed by sampling the continuous signal. This means application of the Nyquist sampling theorem is more of an intuitive approach than one solidly grounded in theory.

The impulse response contains terms for both the echoes from the surface and the line-of-sight signal. As the delay times are referenced to the time-of-arrival of the line-of-sight signal, the delay for the line-of-sight term will be zero. As mentioned in Section 2.1, the time varying gain of the receiver will negate any propagation losses. This means the following assignment can be made.

$$ee_D(0, t_0) = 1 \quad (4.44)$$

The rest of the impulse response is constructed from the facet returns. Each facet has to be assigned to a delay time $n\Delta\alpha$. This is found by simply rounding the facet delay to the nearest delay value.

$$n = \text{round} \left(\frac{v(\hat{x}_0, \hat{y}_0)}{\Delta\alpha} \right) \quad (4.45)$$

The temporal delay $n\Delta\alpha$ has a corresponding phase delay of $\exp[j\frac{2\pi}{\lambda}n\Delta\alpha]$. Thus, when assigning a facet to a delay of $n\Delta\alpha$, the gain is multiplied by $\exp[-j\frac{2\pi}{\lambda}n\Delta\alpha]$. This is because in both the Lambertian model and the diffraction model, continuous-wave (CW) analysis was used but the finite duration of $p(\alpha)$ ensures that the system is not CW. In the CW analysis the delays were represented solely by a phase shift.

When constructing the impulse response used here, delays are made explicit, so a corresponding amount of phase shift should be removed.

Each term of $ee_D(n\Delta\alpha, t_0)$ is found by simply adding all the facets assigned to that delay.

$$ee_D(n\Delta\alpha, t_0) = \sum_{(\hat{x}, \hat{y}) \text{ s.t. } \text{round}\left(\frac{v(\hat{x}, \hat{y})}{\Delta\alpha}\right) = n} G(\hat{x}, \hat{y}) \exp \left[-j \frac{2\pi}{\lambda} n \Delta\alpha \right] \quad (4.46)$$

The gain terms are complex and are added using complex addition. Physically, this corresponds to coherent addition.

Chapter 5

SINGLE SURFACE SIMULATION RESULTS

There are a large number of variables that need to be defined in order to perform a single simulation run. Some of these variables correspond to physical properties of the system while others are related to how the simulation is carried out. In order to gain an intuitive understanding of the system, the results leading to a single multi-path return ($ee_D(n\Delta\alpha, t_0)$) will be investigated. Two cases will be examined, the response from a simulated sea surface and the response from a perfectly flat surface. An intuitive analogy to the multi-path propagation observed is also given. The variables needed to perform the simulation run will now be given, along with an explanation of how they were chosen.

Firstly the sea surface correlation function (Equation 3.3) must be defined. The variables were defined as follows simply because they seemed reasonable for a calm sea surface.

$A_D = 0.2 m$	<i>R.M.S.</i> sea surface displacement
$L_w = 7 m$	Windward correlation length
$L_c = 12 m$	Crosswind correlation length
$L_t = 7 s$	Temporal correlation
$K_w = 1 rad.m^{-1}$	Windward spatial angular frequency
$- = 2 rad.s^{-1}$	Temporal angular frequency
$\psi = 0.7\pi rad$	Wind direction (arbitrary)
$win(\tau)$	Hanning window

Obviously for the flat sea surface none of these parameters were used. The surface

was simply $s(x, y, t_0) = 0$.

The variables D_t , D_r , R and \mathbf{v}_4 define the geometry of a single return (see Figure 4.2.) These will be chosen to be within the design parameters of the KIWI-SAS system and with the target directly in front of the receiver.

$$D_t = 10\text{ m} \quad \text{Target depth}$$

$$D_r = 10\text{ m} \quad \text{Receiver depth}$$

$$R = 100\text{ m} \quad \text{Target range}$$

$$\mathbf{v}_4 = (0, 1, 0) \quad \text{Receiver plane normal}$$

Again following the KIWI-SAS system, the carrier frequency ω_c is chosen to be $2\pi \times 30 \times 10^3 \text{ rad.s}^{-1}$.

The variables already mentioned in this section are ones that correspond to the physical parameters of the system. Several more variables must be defined in order to run a simulation. The sampling periods of the sea surface are $\Delta\hat{x}$, $\Delta\hat{y}$ and Δt . These parameters must be chosen so that the sampled surface adequately represents the real surface it is modeling. This means they depend on the sea surface parameters. The temporal sampling period (Δt) was chosen to be 0.2 s . This is significant over-sampling (for a dominant temporal frequency of 2 rad.s^{-1}) but is on the same order as the KIWI-SAS signalling period. The spatial sampling periods ($\Delta\hat{x}$ and $\Delta\hat{y}$) are very important as they define the facet size. The facets must be small enough to adequately capture the sea surface. In addition, Fraunhofer diffraction assumes that the receiver is in the far field which also means a small facet is desirable. Acting against this is the need for the facet to have dimensions of at least several wavelengths. Fourier optics was applied in the diffraction-based model and this methodology does not hold well for apertures of a size similar to the wavelength. The wavelength λ is determined by the carrier frequency ($\lambda = \frac{2\pi v_s}{\omega_c}$) which in this case gives a wavelength of 5 cm . With these considerations in mind, a sampling period of 50 cm was chosen in both

directions.

The size of the surface to be simulated is limited by computational resources. Through a process of trial and error a suitable size was found. If 128 sample points are taken in the \hat{x} direction (corresponds to a range of 64 m), 384 points in the \hat{y} direction (a range of 192 m) then the surface contains all the significantly contributing facet positions. Temporally, 128 sample points were taken to give a range of approximately 26 s . The sea surface generation code was run with these parameters. As mentioned in Section 3.2, there will be some correlation frequencies that may be considered in error. A function was written to calculate the power in these frequencies. For this particular example, these frequencies represent less than 2% of the total power.

Other parameters that need to be defined are the facet division method (see Section 4.1), the model type (Lambertian or diffraction) and the sampling period of the impulse response ($\Delta\alpha$.) A nominal value for the sampling rate was selected to be 8 times the carrier frequency, i.e. $C_S = \frac{8}{2\pi}$ (see Equation 4.42.)

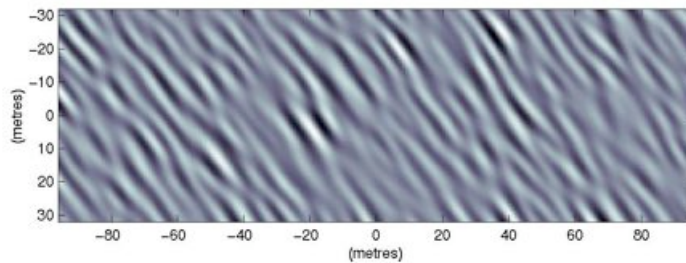


FIGURE 5.1. Example sea surface as an image

The following multi-path results are from a flat surface and from the first temporal slice of sea surface data generated using the parameters above. This sea surface is the one plotted in Figure 3.1 and displayed as an image in Figure 5.1.

5.1 Flat Surface Response

The flat sea surface response is useful in that it is deterministic and represents the mean sea surface state. This allows the underlying trends in the facet gain terms ($G(\hat{x}, \hat{y})$) to be examined. In this section the multi-path results for a flat surface are presented.

One useful tool in doing this is to plot the modulus of the facet-gains as a function of facet position. This results in an image that shows which parts of the sea surface contribute significantly to the impulse response. Each sample point in these images is the coherent sum of a facet and its complementary facet (so the gain-modulus value represents the return from the area between four neighboring sea-surface sample points.)

The delay associated with each facet is a function of position. For a flat surface, the minimum delay will lie on the surface point equidistant from the target and receiver. With the geometry used here the target is at $(0, -50)$ (at a depth of 10 m) and the receiver is at $(0, 50)$ (also at a depth of 10 m), so the minimum delay point is at the origin. Contours of constant delay are ellipses moving out from this point as the delay time increases.

Another advantage of investigating a flat surface is that the simulation parameters can be varied and the results examined. The facet size (determined by $\Delta\hat{x}$ and $\Delta\hat{y}$) will be varied. The assumed wavelength λ will also be varied (because SAS signals are typically wideband and assuming a single λ is not a well justified approximation.)

The resulting impulse response ($ee_D(n\Delta\alpha, t_0)$) will also be constructed and discussed.

5.1.1 Lambertian Model

When a multi-path simulation was run for a Lambertian scattering model on a flat surface, the gain-modulus image of Figure 5.2 was produced. The darker areas rep-

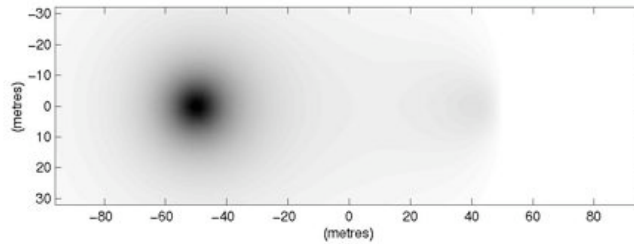


FIGURE 5.2. Gain-modulus image for a flat surface with a Lambertian scattering model

resent a stronger return. The target lies beneath $(0, -50)$ and the receiver is beneath $(0, 50)$. It can be seen that there is a strong return directly above the target and another smaller peak just in front of the receiver. This behavior can be explained by examining the gain expression of Equation 4.21. The dominant terms in this equation are the inner-product expressions. The term $(\mathbf{v}_1 \cdot \mathbf{v}_3)$ corresponds to the solid angle a facet presents to the field originating at the target. This term is at a maximum directly above the target. Similarly, the term $(\mathbf{v}_2 \cdot \mathbf{v}_4)$ corresponds to the solid angle the receiver presents to the return from the sea surface and increases as the facet position moves away from the receiver. The term $(\mathbf{v}_2 \cdot -\mathbf{v}_3)$ corresponds to the Lambertian scattering model — as the path to the receiver moves closer to the facet normal, the scattered return increases. This term increases as the facet position moves closer to the receiver. The net effect of all these factors is the response of Figure 5.2.

It should be noted that when a facet and its complementary facet were added to get a sample point, they were added coherently. However, both facets have the same reference point and as the phase was assigned by propagation distance, both facets have identical phase. This means their complex addition can be described physically as constructive interference. Nearby facets have a similar propagation distance (i.e. propagation distance difference $\ll \lambda$) which means they have a similar phase. Thus the phase varies smoothly across the surface.

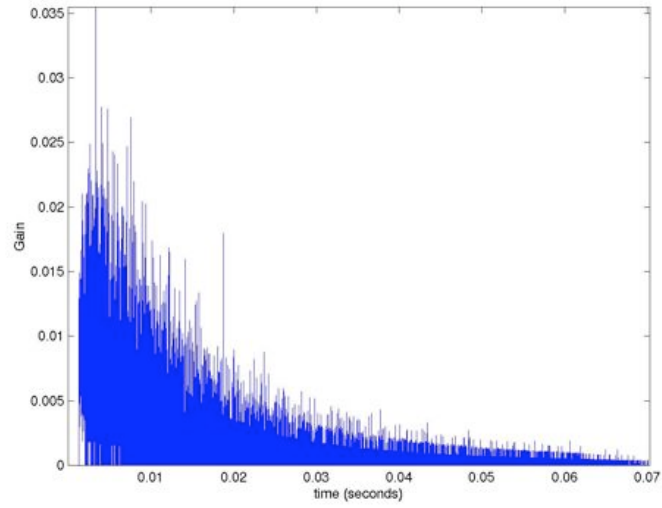


FIGURE 5.3. Modulus of the impulse response for a flat surface with a Lambertian scattering model

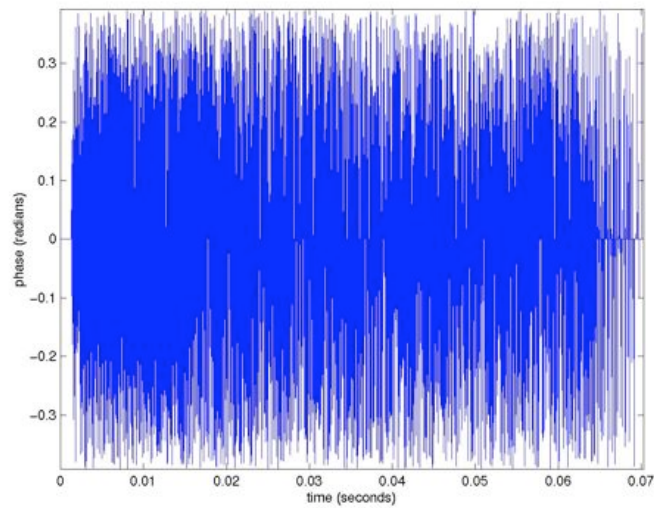


FIGURE 5.4. Phase of the impulse response for a flat surface with a Lambertian scattering model

Figure 5.3 shows the modulus of the resulting multi-path impulse response, while Figure 5.4 is the corresponding phase plot. It should be noted that the first sample point (which always has a value of 1) has not been plotted as doing so makes the range on the vertical axis too large. A gap of about 2 ms can be seen between when the line-of-sight signal arrives and when the first echo responses are registered. This makes sense as the shortest echo path is considerably longer than the direct path from target to receiver. After that gap, a return is observed that has a modulus decaying with time.

Both of the plots appear very noisy. Much of this is due to how the signals are constructed. Facets are assigned (by delay time) to the nearest sample point. A sampling period was chosen (see Section 4.5 for how it is chosen) that resulted in approximately 17000 sample points. With this many sample points, some delays have no facets assigned to them, which results in a gain of 0. This has the potential to make the plots look very noisy. However, for the 2000 samples between the delay times of 2 ms and 10 ms , only 303 have gains of zero.

If the time step in the impulse response is coarsened, there is a potential for the facets to average out to a smoother curve. Doing this would also have the effect of increasing the amplitude of the curve. This result emphasizes the fact that the constructed impulse response ($ee_D(n\Delta\alpha, t_0)$) cannot be thought of as a sampled version of the continuous signal ($ee(\alpha, t_0)$.) How the impulse will effect the final image is dependent upon the transmitted signal $p(\alpha)$. Convolution of $p(\alpha)$ with the impulse response constructed will give an approximation to the actual signal measured at the receiver. This idea can be observed in Equation 2.17. This Equation is formulated so that the multi-path effects change the observable target not the actual image formed; and the range resolution is determined by the transmitted signal — i.e. the transmitted pulse $p(\alpha)$ will ‘smooth’ the target into what is observed. One way of quantifying the effect of the multi-path propagation is to take some sort of energy measure. For this particular case, the *R.M.S.* sum of the facets contributions is 0.435, which is a

significant fraction of the amplitude from the direct propagation (which is 1.)

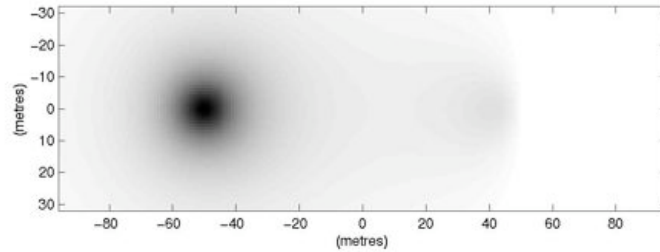


FIGURE 5.5. Gain-modulus image for a flat surface with a Lambertian scattering model and a larger facet size

Figure 5.4 shows a highly variable phase that is distributed between -0.4 and 0.4 radians. This result is logical when the method for assigning phase in the Lambertian model is considered. Phase is assigned to a facet-gain by simply calculating the phase delay over the propagation distance. When the impulse response is constructed these delays are rounded to the nearest delay sample-point and this amount of phase delay is removed from the gain expression. As mentioned earlier, the transmitted pulse should vary little between adjacent delay sample-points. This means the phase delay of the facet and the phase delay of the sample-point it is assigned to should not vary significantly. There will be a small variation however and this corresponds to what is observed in Figure 5.4.

A flat surface is simple and deterministic. In addition, faceting the surface does not introduce any approximation error (the faceted surface is also flat.) For this reason the surface will be sampled at 1 m in both directions and the response examined. Any change in the response is due to the simulation procedure as the surface remains perfectly represented. Intuitive insights are difficult to gain from the impulse response (see Figures 5.3 and 5.4) so the gain-modulus plots will be examined. This neglects phase characteristics, but for the Lambertian case these are well understood.

Figure 5.5 shows the gain-modulus plot for this larger facet size. Comparing it

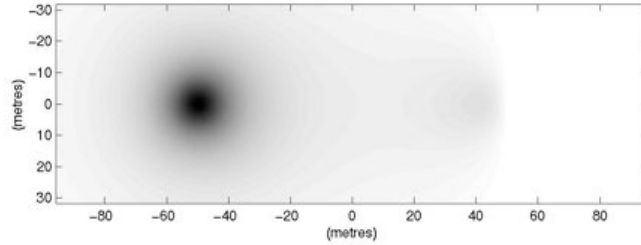


FIGURE 5.6. Gain-modulus image for a flat surface with a Lambertian scattering model and a shorter characteristic wavelength

to Figure 5.2 (the smaller facet size), no differences are evident. This makes sense as the development of the Lambertian model contains no aspects that are sensitive to facet size.

Another simulation parameter that can be varied is the carrier frequency ω_c . A simulation was run with twice the carrier frequency used previously (i.e., ω_c is chosen to be $2\pi \times 60 \times 10^3$.) The gain-modulus image for this simulation is shown in Figure 5.6. Again, there are no noticeable differences. With the Lambertian model, the carrier frequency only effects the phase term. As mentioned earlier in this section, this term is essentially undone when the impulse response is constructed. The phase variance observed in Figure 5.4 does increase. This is a simulation effect but it could be argued that the phase should be more variable for a higher frequency transmitted signal.

5.1.2 Diffraction-Based Model

Figure 5.7 is the gain-modulus image that was produced when a simulation was run on a flat surface with a diffraction-based scattering model. It can be seen that this response is significantly different from the Lambertian case (Figure 5.2.) The Lambertian case is smooth while the diffraction-based case is oscillatory. This is due

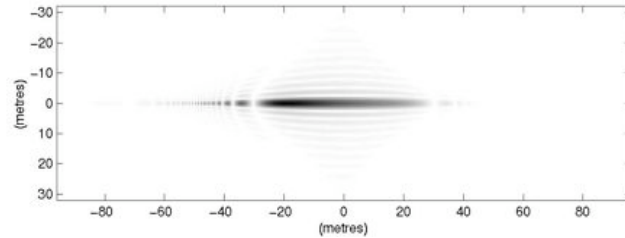


FIGURE 5.7. Gain-modulus image for a flat surface with a diffraction-based scattering model

to the Fourier transform term in the diffraction-based gain equation (Equation 4.40), which tends to dominate the more slowly-varying terms. Since the surface is flat, each facet and its complementary facet add to give a rectangular area. As stated in Appendix A, this results in a separable two-dimensional sinc function for the Fourier transform. The shape of this can be seen in Figure 5.7. The angle between the ray reflection and the path to the receiver are the ordinates of this Fourier transform (see Section 4.4.2.) Thus the area that corresponds to a near direct ray-reflection from facet to receiver (i.e. the central area directly between the target and receiver) has the largest returns. Positions further from this area take on lesser values and tend to oscillate in the same fashion as the two-dimensional sinc function.

Figure 5.7 has been explained in terms of the mathematics of the model but is it reasonable physically? One unlikely property is the lack of smooth contours. The major return from the surface is between the target and the receiver, with smaller responses along the two axes — there are not significant returns on the ‘diagonals’. It seems likely that this phenomenon is a result of choosing triangular facets (that sum to rectangles) rather than any physical property of the real system. A more intuitive response would have elliptical contours of equal return (this sort of result would be produced if the facet’s Fourier transform had circular symmetry.) Another questionable phenomenon is the oscillation in the image — does this seem reasonable?

The impulse response resulting from this surface was constructed. The ampli-

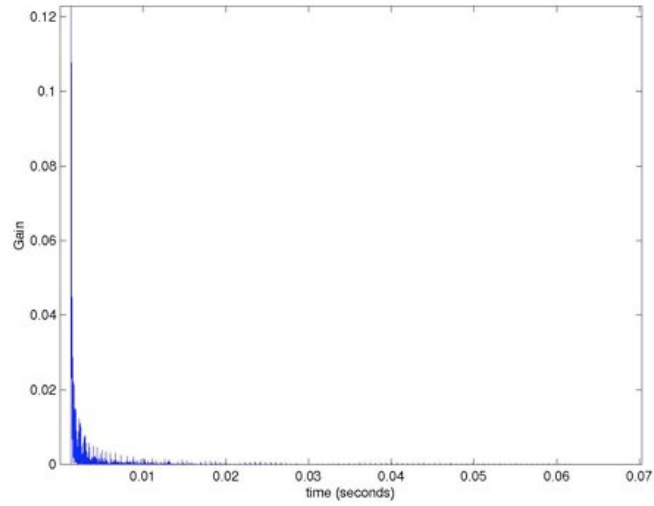


FIGURE 5.8. Modulus of the impulse response for a flat surface with a diffraction-based scattering model

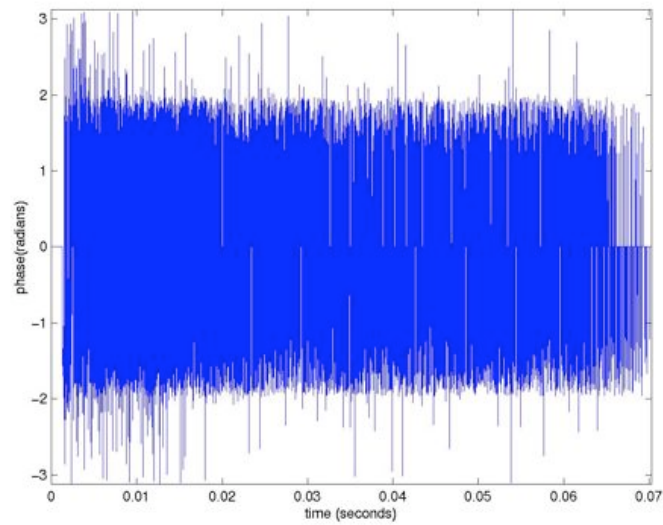


FIGURE 5.9. Phase of the impulse response for a flat surface with a diffraction-based scattering model

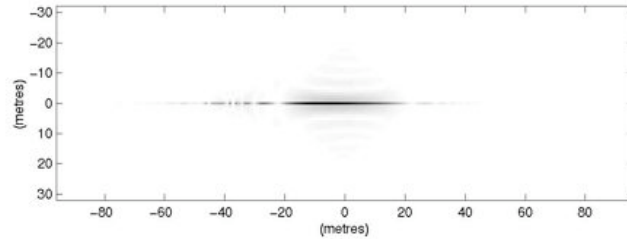


FIGURE 5.10. Gain-modulus image for a flat surface with a diffraction-based scattering model and a larger facet size

tude and phase responses are shown in Figure 5.8 and Figure 5.9 respectively (again, the line-of-sight response is not plotted.) It can be seen that these plots also differ substantially from the Lambertian case. The amplitude response has a higher maximum and the response is concentrated in a shorter time period. Looking at the gain-modulus image of Figure 5.7, this makes sense. The strong returns are concentrated in a small area (with a small range of delay times) and decay rapidly. The *R.M.S.* sum of the returns is 0.348, which is similar to the Lambertian case (and again significant.)

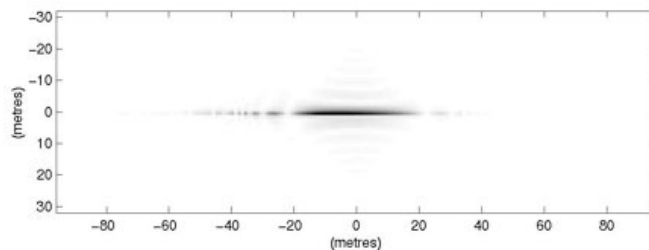


FIGURE 5.11. Gain-modulus image for a flat surface with a diffraction-based scattering model and a larger facet size synthesized by summing smaller facets

The phase of the diffraction model comes from three terms. Firstly there is the phase delay associated with the propagation delay (identical to the Lambertian case), secondly there is a $\frac{1}{j}$ term present and the third contribution comes from the phase

of the Fourier transform term. As mentioned earlier, the flat surface is a special case where the triangular facets add to give rectangular facets. The rectangular facets have a real Fourier transform so the phase must come from the first two terms mentioned above. The $\frac{1}{j}$ term results in a phase of $\pm\frac{\pi}{2}$. Like the Lambertian case, the propagation phase delay only produces a small variance in the phase (as the term is mostly undone when the impulse response is constructed.) Figure 5.9 has a phase response contained mostly within the $\pm\frac{\pi}{2}$ range. The terms that exceed this range occur when two or more facets are added and the variation in the individual phases allows the phase of the sum to exceed the stated range. Like the Lambertian case, the phase here has a predictable structure. However, for the Lambertian case this should be a general result, whereas for the diffraction-based case this only occurs because the surface is flat.

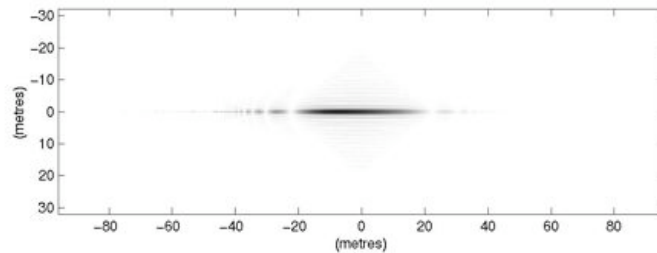


FIGURE 5.12. Gain-modulus image for a flat surface with a diffraction-based scattering and a shorter characteristic wavelength

In order to investigate the simulation reliability, the effects of varying the facet size and the characteristic wavelength were investigated. Figure 5.10 is the gain-modulus image for a flat surface, with a diffraction based model and a facet size of $1\text{ m} \times 1\text{ m}$. This larger facet size results in a more localized response. When the facet size is increased, the corresponding Fourier transform becomes narrower which results in the response observed. Unlike the Lambertian model, the change in facet size produced noticeable changes in the results. However, direct comparison between

the two facet sizes may not be justified. It is possible that the larger facet response can be synthesized by summing smaller facets. This idea appeals to the principal of superposition in a linear system. This approach was tried and the results are shown in Figure 5.11. It can be seen that the response does closely resemble that of the larger facet size. There are differences however — these can be attributed to system non-linearity (i.e. the time-varying receiver gain) and the sensitivity to sampling effects when considering oscillatory signals. This analysis would indicate that the differences inherent in differing facet sizes are not significant. However when a sea surface is considered, differing facet sizes will represent the surface with differing accuracies.

Figure 5.12 shows the gain-modulus image for the diffraction-based model, when the carrier frequency is doubled to $2\pi \times 60 \times 10^3 \text{ rad.s}^{-1}$. The results are similar to what was observed when the facet size was increased. In essence this is what has occurred — the facet size is now larger when compared to the wavelength and this is the ratio that is used in Fourier optics. In fact, by examining the gain equation, an identical result is expected. The differences between the larger facet size image (Figure 5.10) and the shorter wavelength image (Figure 5.12) can be attributed to the difference in image size (in pixels.) The shorter wavelength plot is twice as large and hence allows the main return to appear thicker to the eye. The important result is that the form of the return does vary with wavelength (which is not the case for the Lambertian model.) This means that the assumption of a characteristic wavelength is likely to introduce inaccuracies with the diffraction-based model.

5.2 Sea Surface Response

The response from a simulated sea surface will now be investigated. The particular surface used is that seen in Figures 3.1 and 5.1. The same sorts of investigation methods as used in the previous section will be applied here.

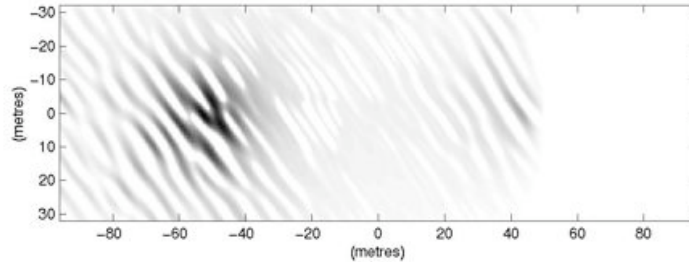


FIGURE 5.13. Gain-modulus image for a sea surface with a Lambertian scattering model

5.2.1 Lambertian Model

Figure 5.13 shows the gain-modulus image for a sea surface with a Lambertian scattering model. This image has the same general trend as the flat surface case (Figure 5.2) but with the wave structure imposing lengths of minimal or zero gain. These structures tend to be more dense away from the area directly between the target and receiver. They can be accounted for by the vector checks of Equation 4.22. As the position moves further away from the receiver, the facet tilt is more likely to produce vectors such that $(\mathbf{v}_2 \cdot -\mathbf{v}_3) < 0$ (i.e. the path to the receiver passes through the surface.) Similarly, as the position moves further from the target, the facet tilt is more likely to produce vectors such that $(\mathbf{v}_1 \cdot \mathbf{v}_3) < 0$ (i.e. the ray strikes the facet from above.) While occlusions are not specifically checked for, it should be noted that both of the above vector checks represent occlusion situations. The *R.M.S.* sum of the contributions is 0.354, which is less than the flat surface response but still significant when compared to the line-of-sight term with amplitude 1.

Plots of the impulse response are shown in Figures 5.14 and 5.15. These responses appear very similar to those for the flat surface case. It should be noted that the range of the phase response is still limited. This seems unlikely when considering real-world scattering from a rough surface.

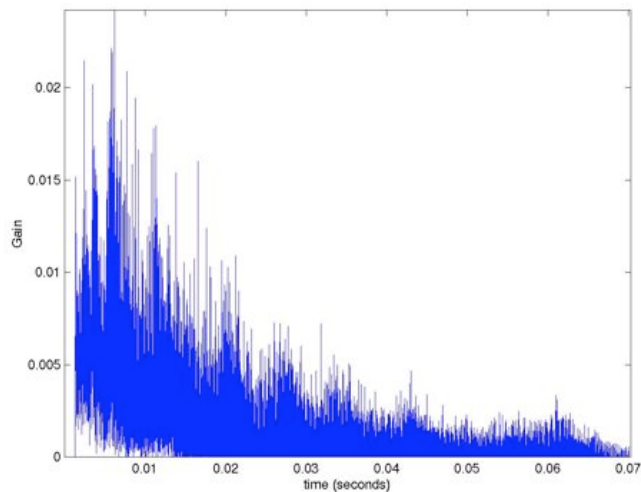


FIGURE 5.14. Modulus of the impulse response for a sea surface with a Lambertian scattering model

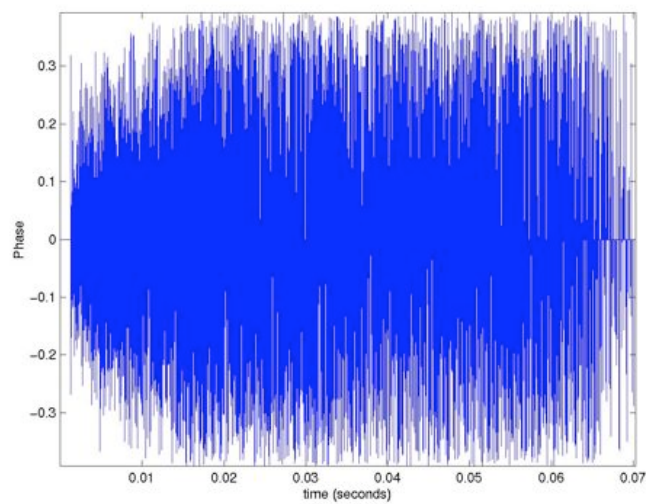


FIGURE 5.15. Phase of the impulse response for a sea surface with a Lambertian scattering model

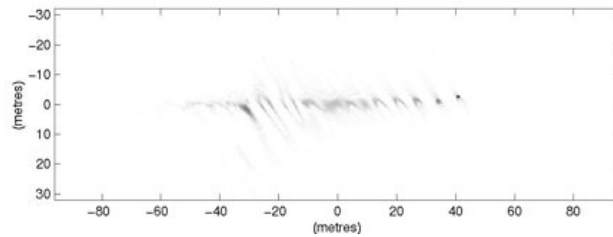


FIGURE 5.16. Gain-modulus image for a sea surface with a diffraction-based scattering model

5.2.2 Diffraction-Based Model

The gain-modulus image for a sea surface using the diffraction-based model is shown in Figure 5.16. It resembles its flat surface counterpart but does have significant effects present attributable to the wave structure. Like the Lambertian case, the tilts of the facets have the effect of reducing the gain in certain places. The *R.M.S.* sum of the contributions is 0.279 — again, less than the flat surface total but still significant.

The impulse response for the sea surface with a diffraction-based model is shown in Figures 5.17 and 5.18. The amplitude response looks similar to the flat surface case, with the significant terms being concentrated early in the response. The phase term is different in that it is random over the whole range of possible values. As mentioned earlier, the phase response of a flat surface with a diffraction-based model represented a special case. As was expected, when a more realistic surface was used, the phase become more random.

5.3 An Intuitive Analogy

It is often instructive to relate a complex problem to an analogous situation for which an intuitive understanding exists. Such an analogy can be developed here by considering the sun at a low level over an ocean surface. The sun emits a wave-field, like the target considered in this investigation. This field is then reflected off the

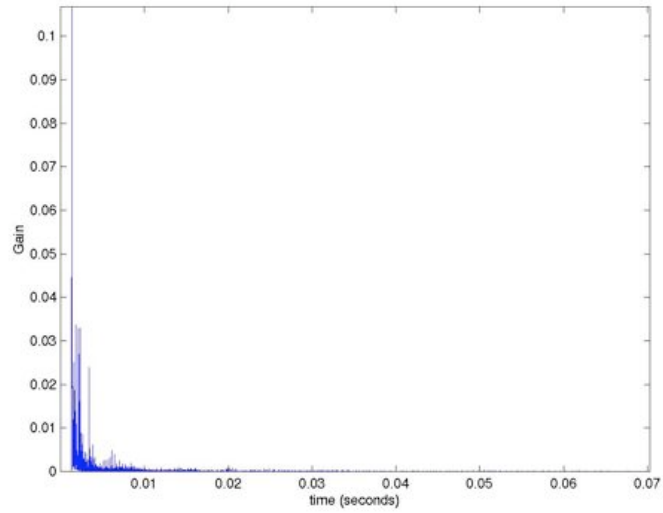


FIGURE 5.17. Modulus of the impulse response for a sea surface with a diffraction-based scattering model

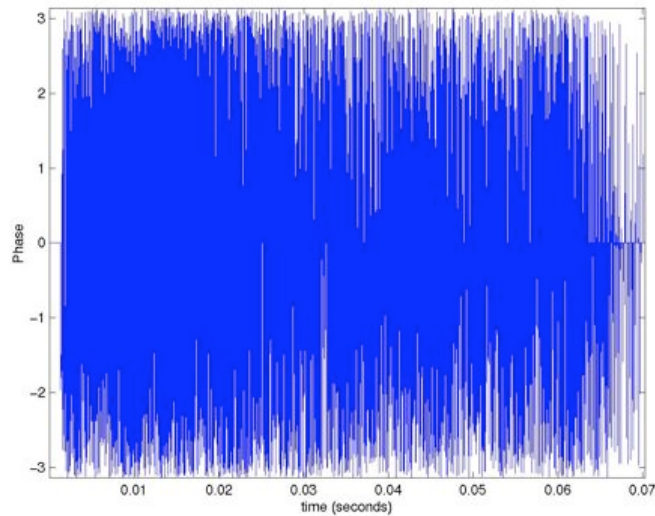


FIGURE 5.18. Phase of the impulse response for a sea surface with a diffraction-based scattering model

sea surface and returned to the receiver — which in the sun-over-sea analogy is the observer’s eye. The glitter pattern observed on the ocean surface is analogous to the gain-modulus plots used extensively in this section.

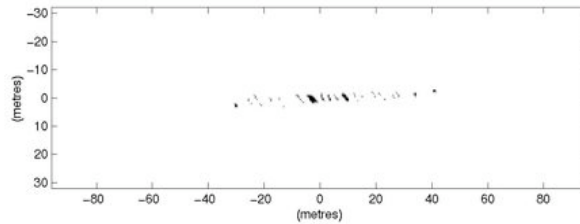


FIGURE 5.19. ‘Glitter’ image for a sea surface

There are a number of differences between the analogy and the problem. Perhaps the most significant is the wavelength of the field. The light observed at optical frequencies has a wavelength in the vicinity of 500 nm (c.f. 5 cm used in this investigation.) At these very short wavelengths the sea surface does not appear rough — i.e. the structure of the sea surface is at a scale far greater than the wavelength. This means that the system can be modeled very accurately by ray optics. Points of glitter are observed where the facet angle is such that the reflected ray is incident on the observer’s eye. This situation was simulated on the example surface used. When the reflected ray path ($\frac{\mathbf{v}_5}{|\mathbf{v}_5|}$) was within a small tolerance of the path to the receiver ($\frac{\mathbf{v}_2}{|\mathbf{v}_2|}$) that facet was marked as a ‘glitter point.’

Figure 5.19 shows the image resulting from this simulation. This response bears a close resemblance to that observed with the diffraction-based model on the same surface. As mentioned in Section 4.4.2, the development of the diffraction-based model results in a facet response that is maximum along the path of a reflected ray. Thus the diffraction-based model bears a resemblance to the ray optics case and hence the sun-over-sea analogy.

The Lambertian results differ significantly from both the diffraction-based model

results and the sun-over-sea analogy. The gain term for the Lambertian model (Equation 4.21) contains no reference to the reflected vector (\mathbf{v}_5) and is generally a smooth function. As it has no narrow dominant function (like the Fourier transform expression in the diffraction-based model) it is more sensitive to the effects of the target's radiation pattern. This is significant because the field from the sun is very accurately represented as a plane wave, however the source from the SAS target is a spherical wave. This represents another major difference between the sun-over-sea analogy and the SAS system. This difference in source characteristics and also in wavelength, means that the sun-over-sea analogy should be applied very cautiously.

5.4 Model Comparison

A basic empirical comparison between the impulse responses reveals some basic properties. Both responses have a set delay gap before multi-path effects contribute. Very soon after this delay gap both responses reach a maximum and then decay with time. The diffraction-based model tends to decay far more rapidly than the Lambertian model but has a similar *R.M.S.* sum of multi-path contributions. The phase response of the Lambertian model is random and restricted to a small range while the phase response of the diffraction model is also random but has a full 2π range.

The gain-modulus images of the Lambertian and diffraction-based models also varied significantly. These images identify areas of the surface that contribute strongly to the multi-path response. The Lambertian images showed a broad, smooth function concentrated on the surface above the target. The diffraction-based model showed a narrow response stretching along the path between the target and receiver. Less significant areas were positioned in a periodic manner adjacent to the main area. The diffraction-based gain-modulus plot looked to have a close relation to that expected from a ray optics model (and the sun-over-sea analogy.)

While the diffraction-based model corresponded closely to a ray optics result,

it's derivation relies on a Fourier optics model. This is satisfying as the model was based on the physics of wave propagation but also produced an intuitive result. The diffraction-based model did have the draw back in that it appeared to be sensitive to the assumed wavelength λ . This wavelength assumption is recognized as a possible source of error and the diffraction-based model results confirm this.

In comparison, the Lambertian model did not correspond to ray optics. The results it produced did seem reasonable however, and the gain-modulus plot was smooth. In addition, the Lambertian model was insensitive to varying the assumed wavelength λ . A counterpoint to this is that the results probably should depend on the wavelength of the signal transmitted. Similarly, the phase of the impulse response was approximately zero, but this does not seem physically reasonable either. It seems very unlikely that the multi-path response should have a predictable phase. The phase of the Lambertian model was added in an ad-hoc manner with the purpose of converting an intensity model (a classical Lambertian reflector) into the amplitude model used here. Assigning a random phase to each facet was investigated. The result was that neighboring facets had no phase correlation and tended to add randomly. This resulted in a gain-modulus image similar to Figure 5.2 but with approximately half of the pixels randomly zeroed. This response did not seem acceptable.

In conclusion, both models had strengths and weaknesses. Although the mechanisms and gain-modulus images of both methods contrasted, the form of the resultant impulse responses was similar. In reality both methods are likely to be significant over-simplifications. Scattering from rough surfaces is a difficult open problem with volumes dedicated to its study (e.g. [11].)

Chapter 6

MULTIPLE SURFACE SIMULATION RESULTS

The previous chapter presented results for a single simulation surface. However, the analysis of Section 2.3 uses the impulse response over the whole ensemble of sea surfaces. A discrete approximation to these impulse responses ($ee_D(n\Delta\alpha, m\Delta t)$) can be easily generated by simply applying the simulation method to successive surfaces.

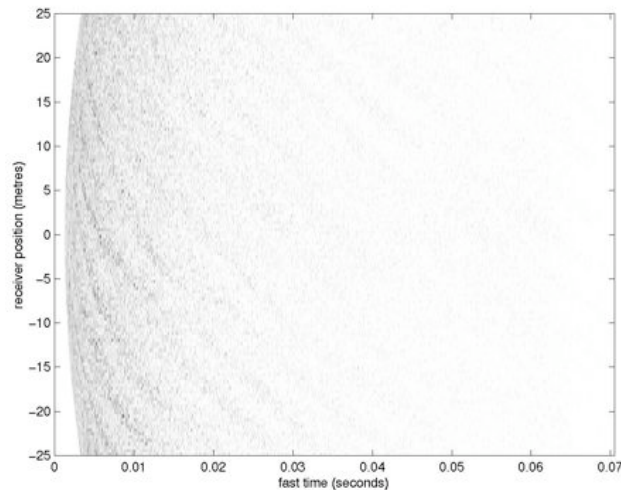


FIGURE 6.1. Set of impulse response magnitudes displayed as an image for sea surfaces with a Lambertian scattering model

As the sea surface evolves, the receiver platform will be travelling along the synthetic aperture path. This means that the distance to the target will change. This effect is modeled by simply changing the range parameter R appropriately at each surface. It may also seem necessary to change the receiver vector \mathbf{v}_4 as the angle to the target varies. This is not the case — the aperture function $A(k_{y'})$ (from Equation

2.6) accounts for this effect. The vector \mathbf{v}_4 is used to calculate the obliquity factor for responses from different facet angles, whereas $A(k_{y'})$ includes the overall obliquity factor from target to receiver.

It should be noted that the above approach does introduce a slight inaccuracy. Simply changing the target range has the effect of producing a rotation in the sea surface. The sea surface is generated on the (\hat{x}, \hat{y}, t) coordinate system where the \hat{y} -axis is defined so that the target and receiver both rely upon it. As the receiver moves, so must the \hat{y} -axis. The sea surface has a directional structure so this produces a slight inaccuracy. To solve this problem would require generating a set of sea surfaces wide enough to support the whole receiver path (from $-Y_0$ to Y_0 .) This was not practical due to computational limitations. In the following simulation examples, the receiver path is from -25 m to 25 m and the target is positioned at 0 m with a range of 100 m . This means the \hat{y} -axis rotates through 30° .

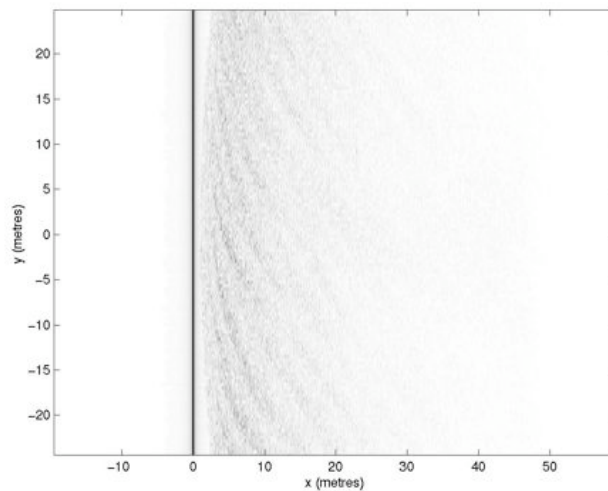


FIGURE 6.2. Set of impulse response magnitudes for sea surfaces with a Lambertian scattering model after Stolt mapping

6.1 Lambertian Model

Figure 6.1 is an image containing the set of impulse response amplitudes for a sea surface with a Lambertian reflector. The first term ($\alpha = 0$) for each impulse has not been included so that the detail of the lower amplitude facet returns is clearly visible. As would be expected, the facet returns start earliest when the target is at its closest to the receiver ($y' = 0$.)

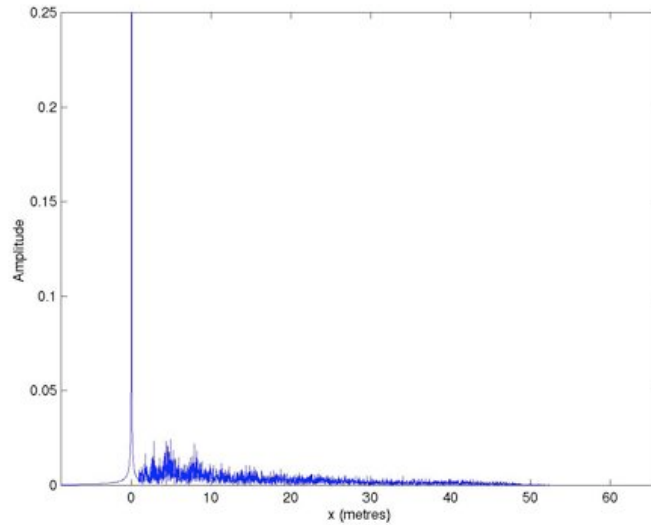


FIGURE 6.3. Target profile when including multi-path effects (Lambertian scattering model)

Section 2.3 makes use of the function $ee(x, y)$ which is found by performing a Stolt mapping of $ee(t, y')$ (Figure 6.1) in the Fourier domain. Figure 6.2 shows the simulated result after performing the Stolt mapping (the image has been clipped at a value of 0.05 so that the high-amplitude line-of-sight term (the vertical line) didn't make the multi-path contributions difficult to see) over the range of frequencies from 10 kHz to 50 kHz . The transmitted signal used in the KIWI-SAS system extends from 20 kHz to 40 kHz , a region that was included in the Stolt mapping.

Figure 6.2 certainly retains the general form of Figure 6.1. By examining Equation

2.20, it can be seen that the effect on the image will be to give the target a x profile given by taking the $y = 0$ slice of Figure 6.2. This profile is shown in Figure 6.3. The line-of-sight term's amplitude is approximately one and the multi-path profile resembles that observed for a single surface in the previous section. The final amplitude of the multi-path profile is determined by the transmitted pulse parameters but (as in the previous chapter) it is significant. Although the amplitude is low at this sample spacing, it has a long duration and an *R.M.S.* sum of 0.209.

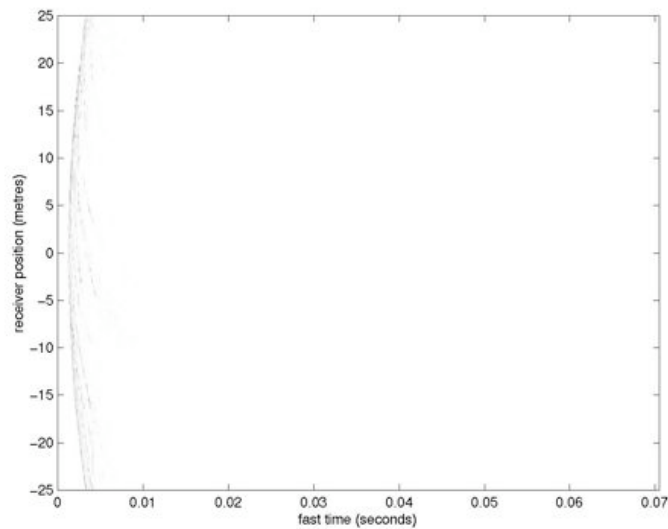


FIGURE 6.4. Set of impulse response magnitudes displayed as an image for sea surfaces with a diffraction-based scattering model

6.2 Diffraction-Based Model

The same results are presented for the diffraction-based model. Figure 6.4 shows the set of raw impulse responses (again with the $\alpha = 0$ term omitted.)

Figure 6.5 shows the results of the Stolt mapping (again an image clipped at 0.05 is displayed and the same 10kHz to 50kHz range is used.) Figure 6.6 gives the final target profile. In this case the *R.M.S.* sum is 0.190. Like the single surface

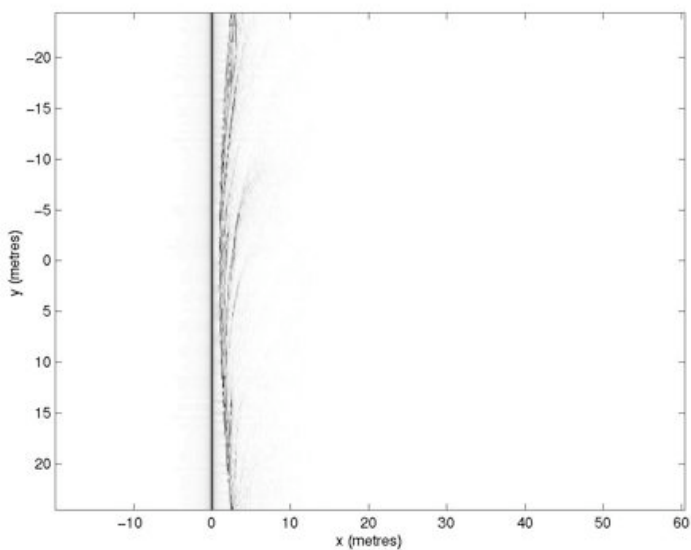


FIGURE 6.5. Set of impulse response magnitudes for sea surfaces with a diffraction-based scattering model after Stolt mapping

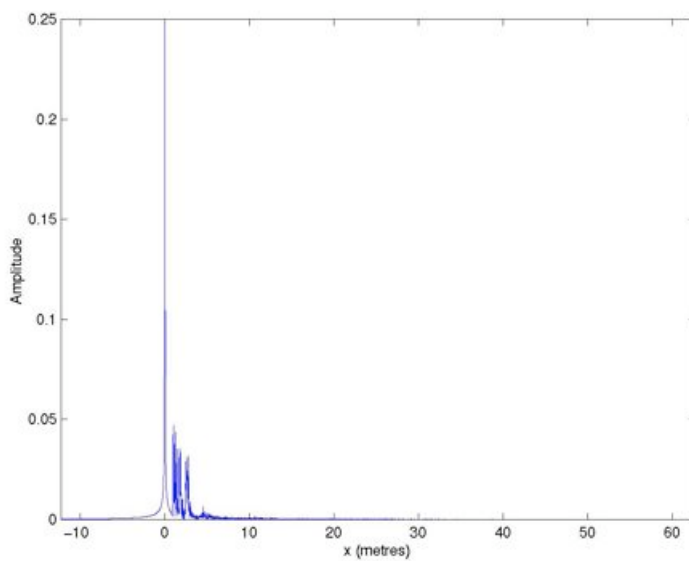


FIGURE 6.6. Target profile when including multi-path effects (diffraction-based scattering model)

results, the main difference between the diffraction-based and the Lambertian models is how quickly the multi-path response decays — the diffraction-based model decays significantly faster.

Chapter 7

CONCLUSIONS

This thesis investigated the effects of multi-path propagation on Synthetic Aperture Sonar systems. The investigation was carried out with a small amount of mathematical analysis but primarily through computer simulation. The multi-path effects investigated involved scattering from a rough surface (the sea surface.) This is a difficult, open problem so a facet-ensemble approach was used to develop a workable simulation method.

Some common, well-understood expressions were derived for the facet model (involving propagation loss, flux calculation, etc.) However, a degree-of-freedom was present in the choice of the facet-scattering model. From physical arguments, two possible models were justified; modeling each facet as a Lambertian reflector and modeling each facet as a diffracting aperture. Results were analysed for both cases and found to produce quite different results.

A particularly insightful technique was to examine which areas of the sea surface produced the strongest returns under the different models. The Lambertian case had a smooth function centered above the target while the diffraction-based model had a narrow reflecting area positioned between the target and receiver. This diffraction-based pattern was found to similar to what would be expected from a ray-optics model.

The Lambertian model was justified by the reasonable assumption that each facet is a rough surface. The diffraction-based model treated each surface as smooth but was a bona-fide amplitude method (whereas the Lambertian model was essentially an intensity method.) The diffraction-based model also gave more believable phase characteristics.

Despite these differences, both models produced returns of the same form — a very rapidly rising and then decaying signal, delayed with respect to the line-of-sight return. The main difference was that the diffraction-based model decayed a faster rate than its Lambertian counterpart. Both models' signals contained significant energy which indicates the effect on the SAS image would also be significant.

This investigation allows some of the artifacts present in SAS images to be accounted for, at least in a qualitative sense. Possible future work could involve thoroughly comparing simulation results and real results. An ideal outcome from this sort of comparison would be a more accurate empirical model. Alternatively, another possible approach is to try to amalgamate the Lambertian and diffraction-based models.

Appendix A

DERIVATION OF THE FOURIER TRANSFORM OF A RIGHT-TRIANGLE

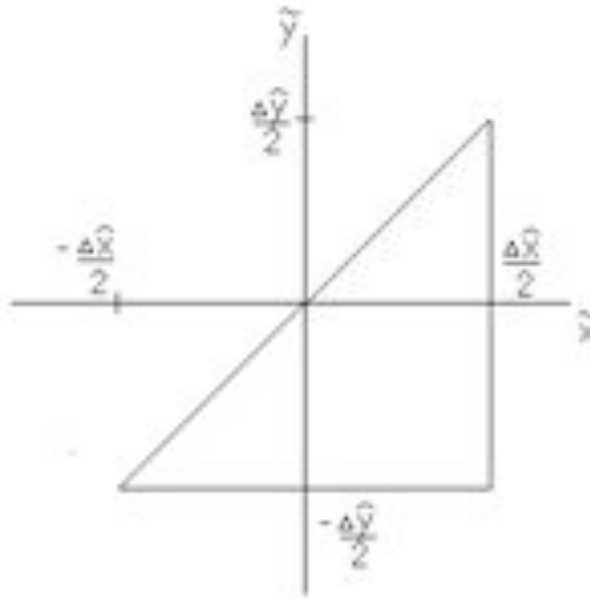


FIGURE A.1. Right-triangle

The function $triangle(\tilde{x}, \tilde{y})$ has an amplitude of 1 inside the triangle shown in Figure A.1 and 0 outside this triangle. This appendix contains the derivation of the Fourier transform of $triangle(\tilde{x}, \tilde{y})$.

$$\begin{aligned}
 F(\omega_{\tilde{x}}, \omega_{\tilde{y}}) &= \int_{-\infty}^{\infty} \int_{-\infty}^{\infty} triangle(\tilde{x}, \tilde{y}) \exp[-j(\omega_{\tilde{x}}\tilde{x} + \omega_{\tilde{y}}\tilde{y})] d\tilde{x}d\tilde{y} \\
 &= \int_{-\frac{\Delta\tilde{y}}{2}}^{\frac{\Delta\tilde{y}}{2}} \int_{\tilde{y}}^{\frac{\Delta\tilde{x}}{2}} \exp[-j(\omega_{\tilde{x}}\tilde{x} + \omega_{\tilde{y}}\tilde{y})] d\tilde{x}d\tilde{y} \\
 &= \int_{-\frac{\Delta\tilde{y}}{2}}^{\frac{\Delta\tilde{y}}{2}} \exp[-j\omega_{\tilde{y}}\tilde{y}] \int_{\tilde{y}}^{\frac{\Delta\tilde{x}}{2}} \exp[-j\omega_{\tilde{x}}\tilde{x}] d\tilde{x}d\tilde{y}
 \end{aligned}$$

Evaluate the inner integral first.

$$\begin{aligned}
 F(\omega_{\tilde{x}}, \omega_{\tilde{y}}) &= \int_{-\frac{\Delta\hat{y}}{2}}^{\frac{\Delta\hat{y}}{2}} \exp[-j\omega_{\tilde{y}}\tilde{y}] \frac{j}{\omega_{\tilde{x}}} [\exp(-j\omega_{\tilde{x}}\tilde{x})]_{\tilde{y}}^{\frac{\Delta\hat{x}}{2}} d\tilde{y} \\
 &= \frac{j}{\omega_{\tilde{x}}} \int_{-\frac{\Delta\hat{y}}{2}}^{\frac{\Delta\hat{y}}{2}} \exp[-j\omega_{\tilde{y}}\tilde{y}] \exp\left(-j\omega_{\tilde{x}}\frac{\Delta\hat{x}}{2}\right) - \exp(-j\omega_{\tilde{x}}\tilde{y}) \Big] d\tilde{y}
 \end{aligned}$$

Split into two integrals.

$$\begin{aligned}
 F(\omega_{\tilde{x}}, \omega_{\tilde{y}}) &= \frac{j \exp\left(-j\frac{1}{2}\omega_{\tilde{x}}\Delta\hat{x}\right)}{\omega_{\tilde{x}}} \int_{-\frac{\Delta\hat{y}}{2}}^{\frac{\Delta\hat{y}}{2}} \exp[-j\omega_{\tilde{y}}\tilde{y}] d\tilde{y} \\
 &\quad - \frac{j}{\omega_{\tilde{x}}} \int_{-\frac{\Delta\hat{y}}{2}}^{\frac{\Delta\hat{y}}{2}} \exp[-j(\omega_{\tilde{y}} + \omega_{\tilde{x}})\tilde{y}] d\tilde{y} \\
 &= \frac{j \exp\left(-j\frac{1}{2}\omega_{\tilde{x}}\Delta\hat{x}\right)}{\omega_{\tilde{x}}} \frac{j}{\omega_{\tilde{y}}} [\exp(-j\omega_{\tilde{y}}\tilde{y})]_{-\frac{\Delta\hat{y}}{2}}^{\frac{\Delta\hat{y}}{2}} \\
 &\quad - \frac{j}{\omega_{\tilde{x}}(\omega_{\tilde{y}} + \omega_{\tilde{x}})} [\exp(-j(\omega_{\tilde{y}} + \omega_{\tilde{x}})\tilde{y})]_{-\frac{\Delta\hat{y}}{2}}^{\frac{\Delta\hat{y}}{2}}
 \end{aligned}$$

Evaluate at both sets of end-points.

$$\begin{aligned}
 &= \frac{-\exp\left(-j\frac{1}{2}\omega_{\tilde{x}}\Delta\hat{x}\right)}{\omega_{\tilde{x}}\omega_{\tilde{y}}} \left[\exp\left(-j\omega_{\tilde{y}}\frac{\Delta\hat{y}}{2}\right) - \exp\left(j\omega_{\tilde{y}}\frac{\Delta\hat{y}}{2}\right) \right] \\
 &\quad + \frac{1}{\omega_{\tilde{x}}(\omega_{\tilde{y}} + \omega_{\tilde{x}})} \times \\
 &\quad \left[\exp\left(-j(\omega_{\tilde{y}} + \omega_{\tilde{x}})\frac{\Delta\hat{y}}{2}\right) - \exp\left(j(\omega_{\tilde{y}} + \omega_{\tilde{x}})\frac{\Delta\hat{y}}{2}\right) \right] \\
 &= \frac{2j \exp\left(-j\frac{1}{2}\omega_{\tilde{x}}\Delta\hat{x}\right)}{\omega_{\tilde{x}}\omega_{\tilde{y}}} \sin\left(\omega_{\tilde{y}}\frac{\Delta\hat{y}}{2}\right) \\
 &\quad - \frac{2j}{\omega_{\tilde{x}}(\omega_{\tilde{y}} + \omega_{\tilde{x}})} \sin\left((\omega_{\tilde{y}} + \omega_{\tilde{x}})\frac{\Delta\hat{y}}{2}\right)
 \end{aligned}$$

Let $\text{sinc}(\sigma) = \frac{\sin(\sigma)}{\sigma}$

$$\begin{aligned}
 F(\omega_{\tilde{x}}, \omega_{\tilde{y}}) &= \frac{j}{\omega_{\tilde{x}}} \Delta\hat{y} \times \\
 &\quad \exp\left(-j\frac{1}{2}\omega_{\tilde{x}}\Delta\hat{x}\right) \text{sinc}\left(\omega_{\tilde{y}}\frac{\Delta\hat{y}}{2}\right) - \text{sinc}\left((\omega_{\tilde{y}} + \omega_{\tilde{x}})\frac{\Delta\hat{y}}{2}\right)
 \end{aligned}$$

Using the Fourier transform property $\mathfrak{F}\{triangle(-\tilde{x}, -\tilde{y})\} = F(-\omega_{\tilde{x}}, -\omega_{\tilde{y}})$ it is easy to find the Fourier transform of the complementary triangle. It is also straightforward to show the following result.

$$F(\omega_{\tilde{x}}, \omega_{\tilde{y}}) + F(-\omega_{\tilde{x}}, -\omega_{\tilde{y}}) = \Delta\hat{y}\Delta\hat{x} \operatorname{sinc}\left(\omega_{\tilde{y}}\frac{\Delta\hat{y}}{2}\right) \operatorname{sinc}\left(\omega_{\tilde{x}}\frac{\Delta\hat{x}}{2}\right)$$

This can be recognized as the Fourier transform of a rectangular function. This property is expected as $triangle(\tilde{x}, \tilde{y}) + triangle(-\tilde{x}, -\tilde{y})$ gives this rectangular function. Using the appropriate Fourier properties, the Fourier transform of any right-triangle can be found from the result presented in this appendix (this obviously includes the right-triangles generated in Section 4.4.2.)

Appendix B

NOTATION GLOSSARY

This appendix contains a glossary of all the variables used and defined throughout this thesis. In the interests of brevity, some generalizations have been made. Functions are only listed as dependent on one set of variables whereas in the text they may have also been written in terms of another set of variables (e.g. the sea surface $s(\hat{x}, \hat{y}, t)$ was also written in windward and crosswind coordinates — $s(w, c, t)$.) The variables listed do not generally include subscripts — for example, k is the spatial frequency found by dividing the temporal frequency ω by the speed of sound, but k_x is a spatial frequency variable in the cross-track dimension (in this listing k is given simply as ‘a spatial frequency variable.’) Also, a function will only be listed in one Fourier space (e.g. $tt(x, y)$ is listed but $Tt(k_x, y)$, $tT(x, k_y)$, $TT(k_x, k_y)$ are not.)

$A(k_{y'})$	SAS Aperture Function
A_D	<i>R.M.S.</i> sea surface displacement
a_r	Receiver area
α	Fast time coordinate
BW	Transmitted signal bandwidth
C_S	Sampling Constant
D_r	Receiver depth
D_t	Target depth
$d(\hat{x}_0, \hat{y}_0)$	Facet’s extra propagation distance

$dd(\alpha, y')$	SAS data received
dS	Infinitesimal surface
$\Delta\alpha$	Fast time sampling period
$\Delta\hat{x}, \Delta\hat{y}$	Sea surface sampling period
$\Delta\hat{z}_{\hat{x}}, \Delta\hat{z}_{\hat{y}}$	Change in sea surface displacement across facet
$ee(\alpha, t)$	Multi-path impulse response
$ee_D(n\Delta\alpha, m\Delta t)$	Discrete time multi-path impulse response
$F(\omega_{\tilde{x}}, \omega_{\tilde{y}})$	Fourier transform of a right-triangle
$FA(\omega_{\tilde{x}}, \omega_{\tilde{y}})$	Fourier transform of a facet
$FAP(\omega_{\tilde{x}}, \omega_{\tilde{y}})$	Fourier transform of a phase-modulated facet
$\mathbf{fe}_{\hat{x}}, \mathbf{fe}_{\hat{y}}$	Facet edge vectors
\mathbf{fe}_{orth}	A vector perpendicular to a facet normal and edge
\mathbf{fn}	Facet normal
\mathfrak{F}	Fourier transform
(ζ, η, τ)	Delay coordinates (windward, crosswind and time)
$G(\hat{x}_0, \hat{y}_0)$	Facet gain
$h(w, c, t)$	Filter used to generate sea surface
$\theta_{\hat{x}}, \theta_{\hat{y}}$	Facet tilt-angles
I	Intensity
$IF(\hat{x}_0, \hat{y}_0)$	Facet incident flux
K_w	Dominant windward spatial frequency

k	Spatial frequency
\square	Facet scattering coefficient
L_c	Sea surface crosswind correlation length
L_t	Sea surface temporal correlation length
L_w	Sea surface windward correlation length
λ	Assumed wavelength
m	Slow time sample coordinate
$m_{\hat{x}}, m_{\hat{y}}$	Facet slopes
$\mu_{\tilde{x}}, \mu_{\tilde{y}}, \mu_{\tilde{z}}$	Direction from target to facet (unit vector)
$N(w, c, t)$	Filtered white noise
n	Fast time sample coordinate
$p(\alpha)$	Transmitted signal
$p_M(\alpha, t)$	Transmitted signal after multi-path effects
$\rho_{\tilde{x}}, \rho_{\tilde{y}}, \rho_{\tilde{z}}$	Direction from facet to receiver (unit vector)
R	Distance between receiver and target
$R_S(\zeta, \eta, \tau)$	Sea surface auto-correlation function
$RF(\hat{x}_0, \hat{y}_0)$	Received flux from facet
r	General range/radius variable
$s(\hat{x}, \hat{y}, t)$	Sea surface
\S	Stolt mapping
σ	Dummy variable

$tt(x, y)$	Target function
$tt_M(x, y)$	Target function after multi-path effects
$triangle(\tilde{x}, \tilde{y})$	Right-triangle function
u_G	Sea surface group velocity
u_P	Sea surface phase velocity
$v(\hat{x}_0, \hat{y}_0)$	Facet's extra propagation time
\mathbf{v}_1	Target to facet vector
\mathbf{v}_2	Facet to receiver vector
\mathbf{v}_3	Upward facet normal
\mathbf{v}_4	Receiver plane normal
\mathbf{v}_5	Reflected ray vector
\mathbf{v}_6	Target to receiver vector
$\tilde{\mathbf{v}}_1$	Target to facet vector (facet-based coordinates)
$\tilde{\mathbf{v}}_2$	Facet to receiver vector (facet-based coordinates)
$\tilde{\mathbf{v}}_5$	Reflected ray vector (facet-based coordinates)
v_s	Speed of sound in water
$\phi_{\hat{x}}, \phi_{\hat{y}}$	Tilt angles of target to facet vector
$\overline{\Psi}$	Rotation matrix (receiver-target to facet-based coordinates)
ψ	Wind direction
φ	Angle between facet normal and path to receiver
(w, c)	Windward and crosswind coordinates

$win(\tau)$	Sea surface auto-correlation window
$W(w, c, t)$	White noise
-	Sea surface dominant temporal frequency
ω	Frequency variable
ω_c	Carrier frequency
(x, y, z)	Receiver-path based coordinates
$(\hat{x}, \hat{y}, \hat{z})$	Receiver and target based coordinates
$(\tilde{x}, \tilde{y}, \tilde{z})$	Facet based coordinates
$\tilde{x}_t, \tilde{y}_t, \tilde{z}_t$	Target position (facet-based coordinates)
$\tilde{x}_r, \tilde{y}_r, \tilde{z}_r$	Receiver position (facet-based coordinates)
x_0, y_0	Target position (receiver-path based coordinates)
$\hat{x}_0, \hat{y}_0, \hat{z}_0, t_0$	Facet position (receiver-target and slow time coordinates)
$\tilde{x}_0, \tilde{y}_0, \tilde{z}_0$	Facet position (facet-based coordinates)
$-Y_0, Y_0$	Receiver path endpoints (receiver-path coordinates)
y'	Receiver position (receiver-path coordinates)

Appendix C

SIMULATION CODE

The simulation code was written completely in the MATLABTM software package. The code is presented in the order in which it is run.

The first function is shown below and generates a matrix containing the auto-correlation function given in Equation 3.3.

```
function [corrmat,xvec,yvec,tvec]=corrfunc()

% Patch size (pixels)
M=128;    %x axis
N=128;    %y axis
T=64;     %t axis

% Physical dimensions
dx=.5;    %metres
dy=.5;    %metres
dt=.2;    %seconds

%Sea State
Lw=7;     %Correlation length - Windward (metres)
Lc=12;    %Correlation length - Crosswind (metres)
Lt=7;     %Correlation length - Temporal (seconds)
K=1;     %Dominant wavenumber - Windward (1/metres)
```

```

W=2;      %Temporal Frequency - (radians/second)
A=0.2;    %RMS wave amplitude - (metres)
O=0.7*pi; %Wind direction - From x-axis (radians)
ug=Lw/Lt; %Group velocity - (metres per second)
uv=W/K;   %Phase velocity - (metres per second)

xvec=[(-(M-1)*dx/2):dx:((M-1)*dx/2)];
yvec=[(-(N-1)*dy/2):dy:((N-1)*dy/2)];
tvec=[(-(T-1)*dt/2):dt:((T-1)*dt/2)];

corrmat=zeros(M,N,T);

for i = 1:M,
    for j = 1:N,
        for k = 1:T,
            x=(i-(M+1)/2)*dx;
            y=(j-(N+1)/2)*dy;
            t=(k-(T+1)/2)*dt;
            w=cos(O)*x+sin(O)*y;      %Go to windward and
            c=sin(-O)*x+cos(O)*y;    %crosswind co-ordinates
            corrmat(i,j,k)=A^2*exp(-((w-ug*t)/Lw)^2)*exp(-(c/Lc)^2)*
            cos((K*w)-(W*t));
        end
    end
end
end

```

```

xwindow=hanning(M);
ywindow=hanning(N);
twindow=hanning(T);
[i,j,k]=ndgrid(1:M,1:N,1:T);
window=xwindow(i).*ywindow(j).*twindow(k);
corrmat=corrmat.*window;

```

A short function was written to calculate the frequencies that were considered in error. It returns the ratio of the power in these frequencies to the total power. This function is given below.

```

function[err,angles,realH2]=err(corrmat)

angletol=.001;    %amount angle can be from zero (between 0 and 1)
[M,N,T]=size(corrmat);

% Zero Pad the correlation function
temp=zeros(2*M,2*N,2*T);
temp((M/2+1):(3*M/2),(N/2+1):(3*N/2),(T/2+1):(3*T/2))=corrmat;
corrmat=temp;

% Calculate the Power Spectral Density
corrmat=fftshift(corrmat);
H2=fft(corrmat,[],1);
H2=fft(H2,[],2);
H2=fft(H2,[],3);

```



```

H2=fftshift(H2);

% Find the dimensionality of the PSD
dim=size(H2);
if length(dim)==2
    dim=[dim,1];
end
D=0;
for j=1:3
    if dim(j)~=1
        D=D+1;
    end
end

% Find the phase of the PSD
% Note, a phase shift of half a pixel must first be undone
% This phase arises because the PSD has even pixel dimensions
[X,Y,Z]=ndgrid(0:(dim(1)-1),0:(dim(2)-1),0:(dim(3)-1));
phase=i^D*exp(-i*pi*(X/dim(1)+Y/dim(2)+Z/dim(3)));
realH2=H2.*phase;
angles=angle(realH2);
angles=abs(angles)/pi;    %between 0 and 1
angles=angletol-angles;  %between angletol and -(1-angletol)
angles=ceil(angles);     %binary mask

```

```

% Calculate the power in the error frequencies

magH2=abs(H2);

err=1-sum(sum(sum(angles.*magH2)))/sum(sum(sum(magH2))) %Measure of 'truncation noise'

```

The following function is used to generate a sea surface from the auto-correlation matrix. This function splits the process into several consecutive sub-processes in order to reduce memory requirements

```

function[yvec,tvec,h,H,H2]=wavegen(corrmat,dy,dt)

[M,N,T]=size(corrmat);

% Output size is a multiple of the size of corrmat
% Size of overall output (M)x(Nx*N)x(Tx*T)
Nx=3;
Tx=2;

yvec=[(-(Nx*N-1)*dy/2):dy:((Nx*N-1)*dy/2)];
tvec=[(-(Tx*T-1)*dt/2):dt:((Tx*T-1)*dt/2)];

% Zero Pad the correlation function to avoid circular convolution
temp=zeros(2*M,2*N,2*T);
temp((M/2+1):(3*M/2),(N/2+1):(3*N/2),(T/2+1):(3*T/2))=corrmat;
corrmat=temp;

% Calculate filter impulse response
corrmat=fftshift(corrmat);
H2=fft(corrmat,[],1);

```

```

H2=fft(H2,[],2);
H2=fft(H2,[],3);
H2=fftshift(H2);
H=sqrt(abs(H2));
H=fftshift(H);
h=ifft(H,[],1);
h=ifft(h,[],2);
h=ifft(h,[],3);
h=fftshift(real(h));
disp('Finished calculating filter impulse response')

% Next few loops create overlapping noise files
% Calculations are split into several files due to computational limits
wnoise=randn(2*M,2*N,2*T);
save noise11 wnoise;
% Extend in y direction (first 'row')
for y=2:Nx,
    newnoise=randn(2*M,2*N,2*T);
    newnoise(1:2*M,1:N,1:2*T)=wnoise(1:2*M,(1:N)+N,1:2*T);
    wnoise=newnoise;
    save(strcat('noise',num2str(y),'1'),'wnoise')
end
% Extend in t direction (first 'column')

```

```

load noise1;

for t=2:Tx,

    newnoise=randn(2*M,2*N,2*T);

    newnoise(1:2*M,1:2*N,1:T)=wnoise(1:2*M,1:2*N,(1:T)+T);

    wnoise=newnoise;

    save(strcat('noise1',num2str(t)), 'wnoise')

end

% Extend in y & t direction (row by row)

for t=2:Tx,

    for y=2:Nx,

        newnoise=randn(2*M,2*N,2*T);

        load(strcat('noise',num2str(y),num2str(t-1)));

        newnoise(1:2*M,1:2*N,1:T)=wnoise(1:2*M,1:2*N,(1:T)+T);

        load(strcat('noise',num2str(y-1),num2str(t)));

        newnoise(1:2*M,1:N,1:2*T)=wnoise(1:2*M,(1:N)+N,1:2*T);

        wnoise=newnoise;

        save(strcat('noise',num2str(y),num2str(t)), 'wnoise')

    end

end

disp('Finished creating noise')

% Perform filtering to create sea surface

for t=1:Tx,

```

```

for y=1:Nx,
    load(strcat('noise',num2str(y),num2str(t)));
    wnoise=fftshift(wnoise);
    WN=fft(wnoise,[],1);
    WN=fft(WN,[],2);
    WN=fft(WN,[],3);
    W=WN.*H;
    w=ifft(W,[],1);
    w=ifft(w,[],2);
    w=ifft(w,[],3);
    w=fftshift(real(w));
    % Take central part (avoid circular convolution effects)
    w=w((M/2+1):(3*M/2),(N/2+1):(3*N/2),(T/2+1):(3*T/2));
    waves(1:M,(1:N)+(y-1)*N,(1:T)+(t-1)*T)=w;
    delete(strcat('noise',num2str(y),num2str(t),'.mat'));
end
end
save waves waves
H=fftshift(H);

```

Now that the sea surface has been created, the next step is to calculate the impulse response. The function that does this calls three lower-level functions. The first of these lower level functions takes a single temporal slice of the sea surface and returns facet tilt angles and positions.

```

function[angleup,anglelow,csurf,cxvec,cyvec]=facets(surface,xvec,yvec)

% Facet division method
method=1;    % Method 0 is an upper right to lower left division
             % Method 1 is an upper left to lower right division
             % Where x is horizontal axis and y is vertical

% Find pixel spacing and surface size
dx=xvec(2)-xvec(1);
dy=yvec(2)-yvec(1);
[M,N]=size(surface);

% Create x-y co-ordinates for centre spots
cxvec=xvec(1:M-1)+dx/2;
cyvec=yvec(1:N-1)+dy/2;

% Create z co-ordinates for centre spots
if method == 0
    for j=1:(M-1),
        for k=1:(N-1),
            csurf(j,k)=(surface(j+1,k+1)+surface(j,k))/2;
        end
    end
end

if method == 1

```

```

for j=1:(M-1),
    for k=1:(N-1),
        csurf(j,k)=(surface(j+1,k)+surface(j,k+1))/2;
    end
end

end

end

% Calculate x and y tilts (in radians)
if method == 1
    for j=1:(M-1),
        for k=1:(N-1),
            a=(surface(j+1,k+1)-surface(j,k+1))/dx;
            b=(surface(j+1,k+1)-surface(j+1,k))/dy;
            angleup(j,k,1)=atan(a);
            angleup(j,k,2)=atan(b);
        end
    end

end

for j=1:(M-1),
    for k=1:(N-1),
        a=(surface(j+1,k)-surface(j,k))/dx;
        b=(surface(j,k+1)-surface(j,k))/dy;
        anglelow(j,k,1)=atan(a);
        anglelow(j,k,2)=atan(b);
    end
end

```

```

        end

    end

end

if method == 0

    for j=1:(M-1),

        for k=1:(N-1),

            a=(surface(j+1,k+1)-surface(j,k+1))/dx;

            b=(surface(j,k+1)-surface(j,k))/dy;

            angleup(j,k,1)=atan(a);

            angleup(j,k,2)=atan(b);

        end

    end

    for j=1:(M-1),

        for k=1:(N-1),

            a=(surface(j+1,k)-surface(j,k))/dx;

            b=(surface(j+1,k+1)-surface(j+1,k))/dy;

            anglelow(j,k,1)=atan(a);

            anglelow(j,k,2)=atan(b);

        end

    end

end

```

The next lower level function handles the calculation of the coordinate rotation associated with the diffraction-based model.


```

function[rotmat,fex,fey]=rotmatcalc(v3,dx,dy)

fn=-v3;

dzx=fn(1)*dx;
dzy=fn(2)*dy;
fex=[dx,0,dzx];
fey=[0,dy,dzy];

feorth=[dx,-(dy*dzx*dzy)/(dy^2+dzy^2),dzx-(dzx*dzy^2)/(dy^2+dzy^2)];
rotmat=[feorth/sqrt(feorth*feorth');fey/sqrt(fey*fey');fn/sqrt(fn*fn')];

```

The final lower-level function calculates the Fourier transform component of Equation 4.40.

```

function[result]=diffield(v2p,v5p,fex,fey,dx,dy,wl,uorl,method);

% uorl=1 indicates the upper triangle

f1=sqrt(fex*fex')/dx*2*pi*(v2p(1)-v5p(1))/wl;
f2=sqrt(fey*fey')/dy*2*pi*(v2p(2)-v5p(2))/wl;

if method==1,
    f1=-f1;
end

if uorl==1,
    f1=-f1;
    f2=-f2;
end

```

```

result=sqrt(fey*fey')/dy*sqrt(fex*fex')/dx*dy*i/fl*(exp(-i/2*f1*dx)*
sinc(dy*f2/2/pi) - sinc(dy/2*(f1+f2)/pi));

% /pi in sinc argument is to account for MATLAB's definition of sinc

```

It is now possible to use these lower level functions in the calculation of the multi-path impulse response. The target's range and depth, the receivers depth, the carrier frequency and the type of model to be used must all be specified.

```

function[h,tauvec,Y,A,glitmat]=impresp(waves,xvec,yvec,R,Dt,Dr,fc,lamb)

% 'lamb' is a Lambertian reflector switch - 1 is on, 0 is diffraction model
memef=1;          % memef=1 ==> a memory efficient method
                  % is used (but outputs A & glitmat are for last surface only)
e=.0015;          % Distance from 1 that cos(angle difference)
                  % can be to be considered direct reflection
vel=1500;         % Speed of sound in water (m/s)
oversamp=4;       % Oversampling of the output (taking fc as base)
dtau=1/2/oversamp/fc; % Sampling period (note fc is in Hertz)
wl=vel/fc;        % Wavelength of signal
method=1;         % See facets.m and check it is the same
v6=[0,R,Dt-Dr];  % Target to receiver vector
v4=[0,1,0];       % Receiver normal vector
Ymin=-25;         % Receiver starting position (target at y=0)
Ymax=25;          % Receiver ending position

[M,N,T]=size(waves);
dx=xvec(2)-xvec(1);

```

```

dy=yvec(2)-yvec(1);
Y=Ymin:(Ymax-Ymin)/T:Ymax;
Y=Y(1:T)+(Ymax-Ymin)/2/T;
Ro=R;                                % R will now represent current range rather
than nominal range

for ll=1:T
    R=sqrt(Y(ll)^2+Ro^2);
    l=ll;
    if memef==1,
        l=1;
    end

    % SURFACE SLOPES AND CENTER POINTS
    [angleup,anglelow,csurf(:,l),cxvec,cyvec]=facets(waves(:,l),xvec,yvec);

    % INITIALIZE OUTPUTS
    glitmatu(:,l)=zeros(M,N);
    glitmatl(:,l)=zeros(M,N);

    for j=1:(M-1),
        for k=1:(N-1),
            % CALCULATE REMAINING SYSTEM VECTORS
            v1=[cxvec(j),cyvec(k)+(R/2),csurf(j,k,l)+Dt];
            v2=[-cxvec(j),-cyvec(k)+(R/2),-csurf(j,k,l)-Dr];

```

```

v3u=[-tan(angleup(j,k,1)),-tan(angleup(j,k,2)),1];
v3l=[-tan(anglelow(j,k,1)),-tan(anglelow(j,k,2)),1];
phix=2*angleup(j,k,1)-atan((csurf(j,k,1)+Dt)/(cxvec(j)+.00001));
phiy=2*angleup(j,k,2)-atan((csurf(j,k,1)+Dt)/(R/2+cyvec(k)+.00001));
v5u=[-1/tan(phix),-1/tan(phiy),-1];
if (v3u*v5u') > 0,      % Forcing the vector to be a true reflection
    v5u=-v5u;
end
phix=2*anglelow(j,k,1)-atan((csurf(j,k,1)+Dt)/(cxvec(j)+.00001));
phiy=2*anglelow(j,k,2)-atan((csurf(j,k,1)+Dt)/(R/2+cyvec(k)+.00001));
v5l=[-1/tan(phix),-1/tan(phiy),-1];
if (v3l*v5l') > 0,    % Forcing the vector to be a true reflection
    v5l=-v5l;
end

% DISTANCE FUNCTION
d(j,k,1)=sqrt(v1*v1') + sqrt(v2*v2') - sqrt(v6*v6');

% UPPER & LOWER REFLECTION VALUES (DIFFRACTION
MODEL)
if lamb==0,
    [rotmatu,fexu,feyu]=rotmatcalc(v3u,dx,dy);
    [rotmatl,fexl,feyl]=rotmatcalc(v3l,dx,dy);
    v2up=rotmatu*v2';

```

```

v2up=v2up'/sqrt(v2up'*v2up);
v2lp=rotmatl*v2';
v2lp=v2lp'/sqrt(v2lp'*v2lp);
v5up=rotmatu*v5u';
v5up=v5up'/sqrt(v5up'*v5up);
v5lp=rotmatl*v5l';
v5lp=v5lp'/sqrt(v5lp'*v5lp);
Au(j,k,l)=(sqrt(v6*v6')+d(j,k,l)/2)^2 * (dx*dy/(2*i*wl)) *
diffield(v2up,v5up,fexu,feyu,dx,dy,wl,1,method)/ (sqrt(v1*v1')^2*
v3u(3)*sqrt(v2*v2')^2*sqrt(v4*v4')*sqrt(v6*v6'))*(v1*v3u')*(v2*v4');
Al(j,k,l)=(sqrt(v6*v6')+d(j,k,l)/2)^2 * (dx*dy/(2*i*wl)) *
diffield(v2lp,v5lp,fexl,feyl,dx,dy,wl,0,method)/ (sqrt(v1*v1')^2*
v3l(3)*sqrt(v2*v2')^2*sqrt(v4*v4')*sqrt(v6*v6'))*(v1*v3l')*(v2*v4');
Au(j,k,l)=Au(j,k,l)*exp(i*2*pi/wl*(sqrt(v1*v1')+sqrt(v2*v2')));
% Add phase
Al(j,k,l)=Al(j,k,l)*exp(i*2*pi/wl*(sqrt(v1*v1')+sqrt(v2*v2')));
% Add phase
end

% UPPER & LOWER REFLECTION VALUES (LAMBERTIAN
REFLECTORS)
if lamb==1,
Au(j,k,l)=(sqrt(v6*v6')+d(j,k,l)/2)^2 * (dx*dy/2/sqrt(pi))
/(sqrt(v1*v1')^2 * sqrt(v2*v2')^(2.5) * v3u(3) *sqrt(sqrt(v3u*v3u')) *

```

```

sqrt(v4*v4') * sqrt(v6*v6')) * (v1*v3u') * (v2*v4') * sqrt(-v2*v3u');
    Al(j,k,l)=(sqrt(v6*v6')+d(j,k,l)/2)^2 * (dx*dy/2/sqrt(pi))
/(sqrt(v1*v1')^2 * sqrt(v2*v2')^(2.5) * v3l(3) *sqrt(sqrt(v3l*v3l')) *
sqrt(v4*v4') * sqrt(v6*v6')) * (v1*v3l') * (v2*v4') * sqrt(-v2*v3l');
    Au(j,k,l)=Au(j,k,l)*exp(i*2*pi/wl*(sqrt(v1*v1')+sqrt(v2*v2')));
% Add phase
    Al(j,k,l)=Al(j,k,l)*exp(i*2*pi/wl*(sqrt(v1*v1')+sqrt(v2*v2')));
% Add phase
end

% MARK UPPER AND LOWER DIRECT REFLECTION PIXELS
cosangleu=(v2*v5u')/(sqrt(v2*v2')*sqrt(v5u*v5u'));
if cosangleu > 1-e,
    glitmatu(j,k,l)=1;
end
cosanglel=(v2*v5l')/(sqrt(v2*v2')*sqrt(v5l*v5l'));
if cosanglel > 1-e,
    glitmatl(j,k,l)=1;
end

% PHYSICAL CHECKS
if (v1*v3u') < 0      % Ray striking facet from above
    Au(j,k,l)=0;

```

```

        glitmatu(j,k,l)=0;
elseif (v2*v4') < 0    % Facet behind receiver
    Au(j,k,l)=0;
    glitmatu(j,k,l)=0;
elseif (v2*v3u') > 0    % >90 degrees between normal and path to
receiver
    Au(j,k,l)=0;
    glitmatu(j,k,l)=0;
end
if (v1*v3l') < 0    % Ray striking facet from above
    Al(j,k,l)=0;
    glitmatl(j,k,l)=0;
elseif (v2*v4') < 0    % Facet behind receiver
    Al(j,k,l)=0;
    glitmatl(j,k,l)=0;
elseif (v2*v3l') > 0 % >90 degrees between normal and path to
receiver
    Al(j,k,l)=0;
    glitmatl(j,k,l)=0;
end

A(j,k,l)=Au(j,k,l)+Al(j,k,l);
glitmat(j,k,l)=glitmatu(j,k,l)+glitmatl(j,k,l);
end

```

```

end

% CREATE IMPULSE RESPONSE
dmax=max(max(d(:,1)));
dd=dtau*vel;
dvec(ll,1:(ceil(dmax/dd)+1))=0:dd:(dmax+dd);
h(ll,1:(ceil(dmax/dd)+1))=0;
for j=1:(M-1),
    for k=1:(N-1),
        tau=round(d(j,k,1)/dd+1);
        h(ll,tau)=h(ll,tau)+A(j,k,1)*exp(-i*2*pi/wl*dvec(ll,tau));
    end
end

h(ll,1)=1;
disp(strcat(num2str(ll),'_of_',num2str(T)))
end

[a,b]=max(max(dvec,[],2));
tauvec=dvec(b,+)/vel;

```

The impulse responses have now been created. The final function performs the Stolt mapping on this set, as shown in Section 2.3.

```

function[ee,xvec,yvec]=eecoord(hset,ypvec,tauvec)

vel=1500;                %Speed of sound

```



```

kmin=2*pi*10000/vel;    %Minimum bandwidth
kmax=2*pi*50000/vel;   %Maximum bandwidth

M=size(ypvec,2);
N=size(tauvec,2);

dyp=ypvec(2)-ypvec(1);
dtau=tauvec(2)-tauvec(1);

%Create ordinates for the Fourier Transform
kyprange=2*pi/dyp;
kyp=[-M/2:(M/2-1)]/M*kyprange;
ktaurange=2*pi/dtau;
ktau=[-(N-1):(N-1)]/(2*N-1)*ktaurange;
k=ktau/vel;

disp('Taking Fourier Transform')
hsetzp=[zeros(M,N-1),hset];
Hsetzp=fftshift(fft2(fftshift(hsetzp)));

% Find Area to work in
m=find((k>=kmin) & (k<=kmax));
Hsetzp=Hsetzp(:,m);
k=k(m);
dk=k(2)-k(1);
kN=size(k,2);

```

```

%Find output FT ordinates

ky=kyp;

kxmin=2*k(1);

kxmax=sqrt(4*k(kN)^2-kyp(M)^2);

kx=kxmin:dk:kxmax;

kxN=size(kx,2);

EE=zeros(M,kxN);

disp('Performing Stolt Mapping')

for n=1:M,

    kstolt=sqrt(4*k.^2-kyp(n)^2);

    EE(n,:)=interp1(kstolt,Hsetzp(n,:),kx,'*cubic');

end

disp('Taking output back to Spatial Domain')

ee=ifftshift(fft2(ifftshift(EE)));

%Create output ordinates

xrange=2*pi/dk;

xvec=[-kxN/2:(kxN/2-1)]/kxN*xrange;

yvec=ypvec;

```

REFERENCES

- [1] D.W. Hawkins and P.T. Gough, “Recent sea trials of a synthetic aperture sonar,” *Proceedings of the Institute of Acoustics*, vol. 17, no. 8, pp. 1–10, December 1995.
- [2] D.W. Hawkins, *Synthetic Aperture Imaging Algorithms: With Application to Wide Bandwidth Sonar*, Ph.D. thesis, Electrical and Electronic Engineering, University of Canterbury, Christchurch, New Zealand, October 1996.
- [3] J.C. Novarini and J.W. Caruthers, “Numerical modeling of acoustic-wave scattering from randomly rough surfaces: An image model,” *The Journal of the Acoustical Society of America*, vol. 53, no. 3, pp. 876–884, 1973.
- [4] J.C. Novarini and H. Medwin, “Diffraction, reflection, and interference during near-grazing and near-normal ocean surface backscattering,” *The Journal of the Acoustical Society of America*, vol. 64, no. 1, pp. 260–268, July 1978.
- [5] W.A. Kinney, C.S. Clay, and G.A. Sandness, “Scattering from a corrugated surface: Comparison between experiment, Helmholtz-Kirchoff theory, and the facet-ensemble method,” *The Journal of the Acoustical Society of America*, vol. 73, no. 1, pp. 183–194, January 1983.
- [6] P.T. Gough and D.W. Hawkins, “Unified framework for modern synthetic aperture imaging algorithms,” *The International Journal of Imaging Systems and Technology*, vol. 8, pp. 343–358, 1997.
- [7] Mehrdad Soumekh, *Fourier Array Imaging*, Prentice Hall, Englewood Cliffs, New Jersey, 1994.
- [8] H. Medwin and C.S. Clay, *Fundamentals of Acoustical Oceanography*, Applications of Modern Acoustics. Academic Press, San Diego, California, 1998.
- [9] J.R. Schott, *Remote Sensing: The Image Chain Approach*, Oxford University Press Inc., New York, New York, 1997.
- [10] J.W. Goodman, *Introduction to Fourier Optics*, Electrical and Computer Engineering: Electromagnetics. McGraw Hill, New York, New York, 2nd edition, 1968.
- [11] P. Beckmann and A. Spizzichino, *The Scattering of Electromagnetic Waves from Rough Surfaces*, Macmillan, New York, New York, 1963.